# "Study of long term X-ray time lags in AGN"

Department of Physics,

University of Crete


**Master Thesis**

*submitted for the degree of*

**Master of Science**

by

Angelos Karakonstantakis

Supervisor: Prof. I. Papadakis

Committee members: Prof. N. Kylafis and Dr. P. Reig

September 10th, 2021

**Abstract**

The X-ray emission from AGN is highly variable, on short (minutes/hours/day) and long (months/years) time scales. A particular characteristic of the observed variations is that the higher energy band variations are delayed with respect to lower energy photons. I will use archival *Rossi X-ray Timing Explorer (RXTE)* light curves and I will study the long term, frequency-dependent, X-ray time-lags of the Seyfert galaxies MCG-6–30–15, Ark 564 and Mkn 766 in the 2–4, 4–7, and 7–10 keV bands. The main objective of this project is to investigate how these delays compare with the results from the model fitting of the time lags at higher frequencies.

# Contents

# Chapter 1: Introduction

## 1.1 Active Galactic Nuclei

An *Active Galactic Nucleus* (AGN) is a region at the center of a galaxy, which emits an enormous amount of energy (i.e. $10^{9-15}L_{\odot}$) in a tiny (astronomically speaking) volume (smaller than $\sim$ hours/days/weeks radii, as determined by variation changes). Continuum emission from AGN covers the whole electromagnetic spectrum, from radiowaves all the way to X-rays and $\gamma$ rays. Various characteristics of the AGN spectra suggest that the emitted luminosity is not produced by stars. For example, we see broad and narrow emission lines in the optical spectrum of an AGN (which are usually absent in regular galaxies spectra). Additionally, the intense emission in radio-waves and X-rays is not observed in normal galaxies. Apart from these spectral characteristics, hundreds of thousands of O-type stars would be required to emit the enormous UV luminosity which is observed from such a small region of a few light days (as determined by the UV observed variations). At such high stellar densities the system will collapse to a BH due to frequent collisions (Rees, 1984).

The emission from an AGN is believed to be the result of accretion into a supermassive (typically $10^6$–$10^{10}M_{\odot}$) black hole (BH) at the center of the host galaxy. Approximately 43% of the galaxies in the nearby universe host an active nucleus (Ho et al., 1997). It is possible that every galaxy goes through an active phase in its lifetime at least once. If all the the galaxies we observe host a BH, the fact that we observe a percentage of galaxies in an active state could mean that galaxies become active for a certain period of their lifetime.

Active galaxies come in a variety of types, including Seyfert galaxies, quasars, radio galaxies and blazars. These types were discovered separately and at first seemed they were intrinsically different objects. However, a unified model has been developed the last decades, classifying AGN in different classes considering changes in only a small number of parameters such as orientation and the presence of jets. "Radio-quiet" AGN, i.e. AGN without a relativistic jet, can be divided in two main classes namely, "Type 1/Type 2" objects. The main observed difference, is the presence/absence of broad emission lines in the optical band. According to the current unification schemes, the central engine in "Type 1" AGN is observed directly with minimal obscuration, revealing the presence of gas clouds orbiting the central engine at high angular frequency that produce broad emission lines, due to Doppler broadening (velocities inferred by the broadening of the lines are up to $10000km/s$). On the other hand, "Type 2" AGN are observed at high inclination angles ($\geq$40°). In this case, it is believed that a dusty torus surrounding the cental engine, obscures the gas orbiting the central BH at high velocities. The observed emission lines in "Type 2" AGN are narrow (velocities $< 1000km/s$), and originate mostly from gas existing far away from the center where the orbital velocities are low. In this work, we deal with three Type 1 radio-quiet Seyfert AGN.

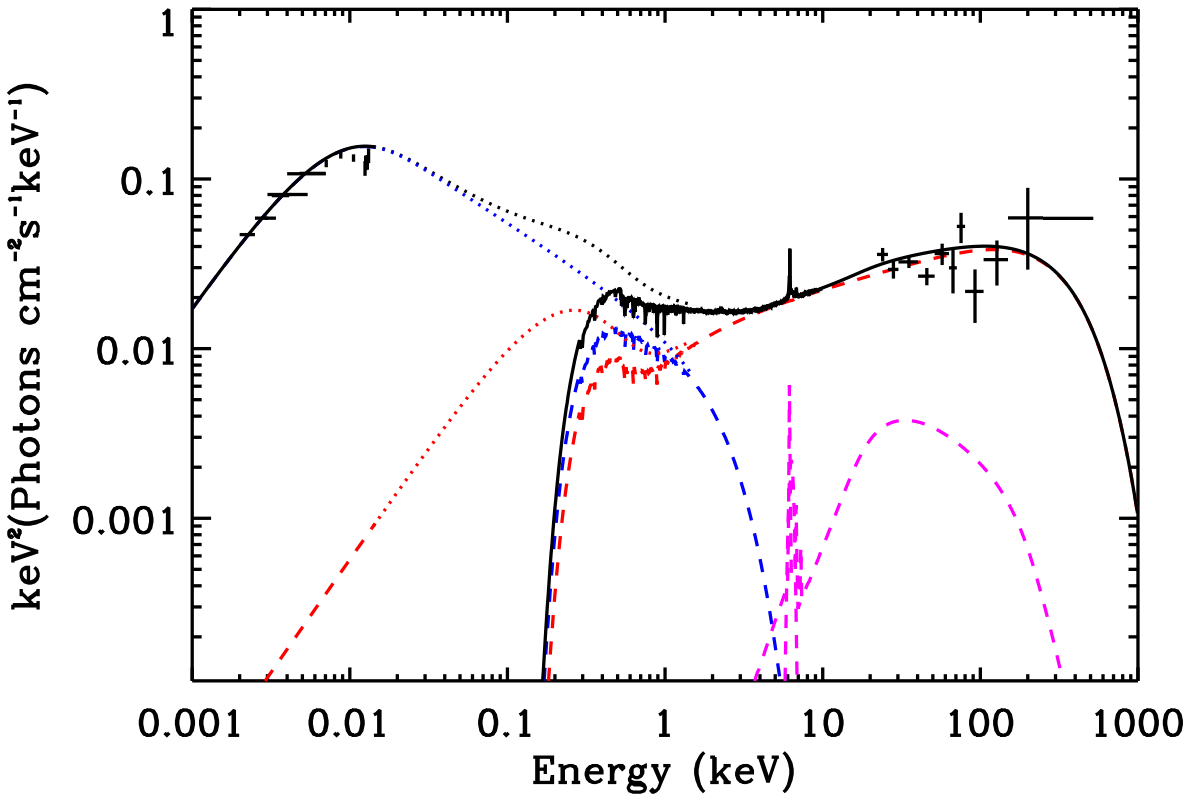


**Figure 1.1:** The broad band spectrum of Mkn 509 which is a typical AGN (figure taken from Petrucci et al., 2013).

### 1.1.1 The emitted spectrum

AGN emit radiation over the whole spectrum of electromagnetic radiation. The emission in different spectral bands is produced by different radiative mechanisms. For example, the optical/UV luminosity is due to black-body emission from the accretion disc. The infrared luminosity is due to emission from hot, dusty material, located far away from the center, which absorbs light emitted from the accession disc. X-rays are produced in a hot plasma, via inverse Compton scattering of the optical/UV photons emitted by the disc. Finally, $\gamma$-rays are detected from "radio-loud" AGN and are emitted from jets of particles that move with relativistic speed.

Fig. (1.1) shows the spectrum from a galaxy called Mrk 509, which is a typical radio-quiet AGN. The observed data are marked with the black crosses. Lines of various colors and the solid black line show the emission of various model components and the overall best-fit theoretical model, respectively. At energies lower than $\sim 10^{-2} keV$ (i.e. in the optical/UV band) the flux increases with increasing photon energy as, $F_\nu \propto \nu^{0.7}$. This behavior is typical in AGN. It is called "big blue bump" and is a defining characteristic of AGN as it is not observed in normal galaxies. We currently believe that photons emitted by the disc are upscattered to higher energies (X-ray) via Inverse Compton scattering. The spectrum in high energies has a power-law shape up to a cut-off energy, of the order of $\sim$ 200keV in this object. This cut-off energy is though to be representative of the electron temperature in the hot plasma that comptonizes the soft photons. The hot electrons are unable to transfer energy to the disc soft photons, larger than their kinetic energy.

#### X-ray emission from AGN

In this work we deal with the X-ray emission of AGN. X-ray luminosity in the 2–10 keV band corresponds to $\sim$ 10% of the bolometric luminosity of AGN (Lusso et al., 2012). According to the

current paradigm, electrons are heated, by a yet unknown mechanism, in a region which is called "corona". Photons emitted by the disc, enter the corona and by interacting with the electrons in the corona, are upscattered to higher energies by Inverse Compton scattering. As discussed before, the primary X-ray emission is characterized by a power-law spectra shape extended up to energies determined by the temperature of the corona. Akylas and Georgantopoulos (2021) studied hundreds of AGN using *NuSTAR* observations and they found that the photon index[1] varies between 1.2–2.4. The median value of the photon index distribution is $\Gamma = 1.77$. They also measured the high energy cut-off which is proportional to the electron temperature in the corona. The mean value in their sample is at $\sim$ 100keV.

Apart from the power law continuum, Fig. (1.1) reveals several other interesting observational features in the X-ray spectra of AGN. One of these features is the characteristic excess on top of the power-law emission at soft X-rays below $\sim$ 1–2keV. This is the so-called "soft excess" component (Arnaud et al., 1985) which is observed in more than 50% of Type 1 AGN. "Soft excess" is modeled by the blue dashed line in Fig. (1.1). Its origin is a matter of debate in the scientific literature. The most commonly used models are blurred ionized reflection (e.g. Crummy et al., 2006) and Comptonization of disc photons by a "warm" corona (e.g. Done et al., 2012). Another observational characteristic of AGN is the presence of emission lines, the most prominent of which is the iron K$\alpha$ emission at around 6.4keV. Additionally, the magenta dashed line represent the so-called Compton hump (or reflection hump), which is observed at around 30 keV. This feature corresponds to Compton down-scattering of the high energy power-law continuum emission by low energy electrons in the accretion disc.

The X-ray emission from AGN is highly variable. The X-ray flux in AGN shows the fastest, and largest amplitude than any of the wavelength ranges. The sources vary both in flux and in spectral shape. In many objects we observe variations over time scales as short as one hour. The short X-ray variability time scales indicate that the X-ray emission originates from a very compact region ($\sim 1lh \simeq 10AU$[2]). This has been confirmed by studies that used gravitational microlensing technics in distant quasars to deduce that the X-ray emitting region can be as small as $\sim 10R_g$ (Chartas et al., 2016). Where, $R_g$ is the gravitational radius and for a compact object of mass $M$ is defined as $R_g = GM/c^2$. For a typical BH mass of $M = 10^8 M_\odot$, $R_g \simeq 1.5 \times 10^{13} cm \sim 1AU$. Thus, the emitting region of $10R_g$ corresponds to $\sim 10AU$. The physical mechanism behind the variability still remains unknown. Nevertheless, X-ray variability studies can provide valuable information that can be used to understand the nature and the physical characteristic of the X-ray emitting region.

## 1.2 Correlation between variations in different X-ray energy bands

The study of correlation between light curves in different energy bands has been the subject of active research in the past years. As an example, Papadakis and Lawrence (1995) performed one of the first such variability study in AGN. They used observations of the Seyfert galaxy NGC 4051, taken by the "European X-ray Observatory Satellite", `EXOSAT`. The left panel of Fig. (1.2) shows light curves of NGC 4051, normalized to their mean, in a low energy band of 0.05–2 keV and in 2–10 keV band. The figure shows a good corelation between the variations detected in two bands. The 2–10 keV energy band appears to be slightly delayed compared to 0.05–2 keV band. In order to investigate the correlation between the two energy bands, the authors estimated their cross-corelation function (CCF; see Chapter 3). The CCF is plotted at the right panel of Fig. (1.2). The observed CCF shows a steep narrow peak at 0. This indicates that the variations in the two bands are well correlated with no delays.

[1]The photon index, $\Gamma$, is the slope of the spectrum in units of photons $s^{-1}cm^{-2}keV^{-1}$.

[2]An astronomical unit (AU) is the mean distance from earth to the sun.

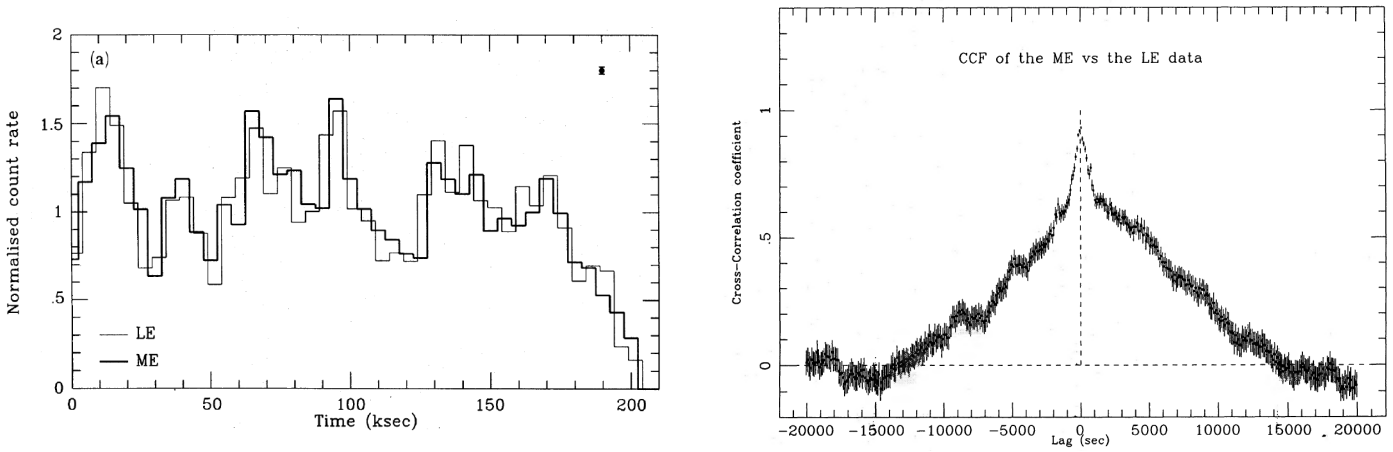


**Figure 1.2:** (Left panel): Light curves of NGC 4051 in the 0.05–2keV band (thin line) and in the 2–10keV band (bold line). Light curves are normalized to their average value. (Right panel): The cross-corelation coefficients between the two light curves (figures taken from Papadakis and Lawrence, 1995).

However, if we ignore the lags between $\sim -1000s$ and $+1000s$, the plot appear to be asymmetric at 0. The center of the plot appears to be shifted to the positive lags, indicating that the variations in the 2–10 keV band are delayed compared to the variations in 0.05–2 keV band.

More recent studies of AGN utilize a different analysis technic for X-ray time-series. A rather powerful variability analysis tool is the so-called "time-lags" of the temporal variations between different energy bands. This kind of analysis is performed in the frequency domain rather than the time-domain. In that way, it is easier to describe the underlining structure of a variable process by measuring the time differences (time-lags) of the sinusoidal components at each Fourier frequency.

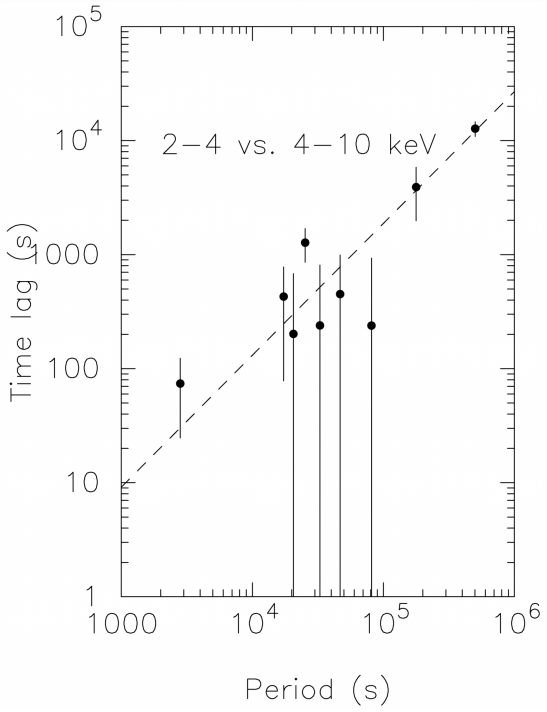


**Figure 1.3:** Time-lags as a function of the Fourier period $(1/f)$ between the 2–4 keV and 4–10 keV bands of NGC 7469. The dashed line indicates the best power law model fit. The slope of the fit is $1.2 \pm 0.2$ and the normalization $2.6 \times 10^{-3}s$ (figure taken from Papadakis et al., 2001).

The first of such studies were performed for BH X-ray binaries systems (BHXBs; e.g. Miyamoto and Kitamoto, 1989; Nowak and Vaughan, 1996; Nowak et al., 1999; Pottschmidt et al., 2000). BHXBs are accreting systems where the one of the companions is a BH with a $M_{BH} \sim 10 M_{\odot}$ (in AGN, $M_{BH} \sim 10^{6-10} M_{\odot}$). According to those studies, variations in the hard energy bands are delayed with respect to the variations in softer energy bands.

Similar results were later reported in AGN, which supports the arguments that the X-ray variability mechanisms in AGN and BHXBs are similar. The first time-lag study in AGN were performed by Papadakis et al. (2001). Fig. (1.3) shows their results. The figure shows time-lags in the X-ray emission between the 4–10 keV and 2–4 keV bands of the Seyfert galaxy NGC 7469. The time-lags increase with increasing Fourier period and are well fitted by a power law of slope $\sim 1$ (indicated by the dashed line). Later, many more studies were performed in AGN including McHardy et al. (2004), Arévalo et al. (2006), Arévalo et al. (2008), Sriram et al. (2009).

Recently, Epitropakis and Papadakis (2016, hereafter `EP16`) developed, for the first time prescriptions for reliable estimates of the time-lags. Later, they applied those technics to estimate the time-lags between various bands from 0.3 to 10 keV and the 2–4 keV band of 10 bright and highly variable AGN observed by the `XMM-Newton` (Epitropakis & Papadakis, 2017, hereafter `EP17`). Their main results are the following: (i) Time-lags are well fitted by a power law slope of $\sim -1$ between light curves at all energy bands. This value is consistent with all AGN in `EP17` sample except Mkn 766 in which the best fitting plot is consistent with zero. (ii) The time-lags increases logarithmically with the ratio of the mean energy of the used light curves energy bands. (iii) The normalization is positively correlated with the X-ray Eddington ratio. Fig. (1.4) shows the time lag normalization as a function of the X-ray Eddington ratio ($\lambda_X = L_X/L_{Edd}$), the ratio between the X-ray luminosity and Eddington's luminosity[3]. The data are well fitted by a power law of the form: $A_0 = (3.42 \pm 0.13)\lambda_X^{(0.55\pm0.07)}$ i.e. the time-lags are proportional to the square-root of the Eddington ratio.

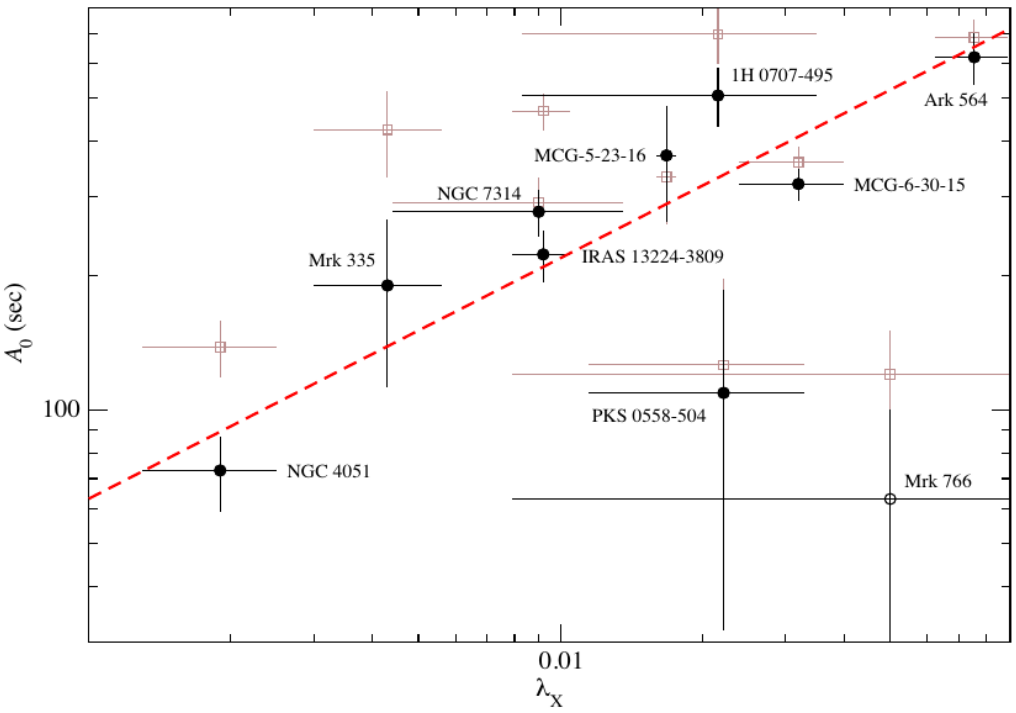


**Figure 1.4:** The time-lag amplitude as a function of the Eddington ration. The red dashed line represents the best fitting power law model to the data (figure taken from `EP17`).

[3]Eddington luminosity, $L_{Edd}$, of a stellar object of mass $M$ is the luminosity in which the gravitational pressure (acting inwards) equals the radiation pressure (acting outwards) and is given by: $L_{Edd} = 4\pi G M m_p c/\sigma_T$, where, $G$ is the gravitational constant, $m_p$ is the proton's mass, $c$ is the speed of light and $\sigma_T$ is the Thomson cross section.

## 1.3 The main objective of this work

Recently, Papadakis et al. (2019) estimated the time-lags between the 2–4, 4–7 and 7–10keV bands of the Seyfert galaxy NGC 4051 using data from the *Rossi X-ray Timing Explorer (RXTE)*. They measured time-lags between $10^{-7}$–$10^{-6}Hz$ which is the lowest frequency range that have ever been measured in AGN. They combined their results with the results of `EP17` for NGC 4051 at the same energy bands but at higher frequencies. The open circles in Fig. (1.5) show their results. The black line show the `EP17` best fit and its extrapolation at low frequencies. The dashed lines show the $1\sigma$ uncertainty of the slope and normalizations of the `EP17` best fit. The continuum time-lags of NGC 4051 at low frequencies are consistent with the best power-law fit of `EP17` with a slope of $\sim -1$.

The main aim of this work is to compute the low frequency time-lags in three more Seyfert 1 AGN and to further study the relation between the low and high frequency time-lags in AGN. To this end we choose to study three more radio-quiet Seyfert 1 galaxies, namely MCG-6–30–15, Ark 564 and Mkn 766. These are X-ray bright and highly variable objects that have been studies extensively by *RXTE*. Therefore, we can use archival *RXTE* data, to compute the time-lags between 2–4keV (the reference band) and the 4–7/7–10 keV bands. The *RXTE* light curves of the three sources are divined into parts and the construction of equidistant light curve parts is discussed in detail in Chapter 2. In Chapter 3, we present the statistical tools needed for the study of the temporal corelation between the different light curves following `EP16` prescriptions. In the same chapter, we present the results from the time-lag analysis. In Chapter 4, we compare our results with the result of `EP17` at higher frequencies and finally, Chapter 5 summarizes the results and conclusion of this work.

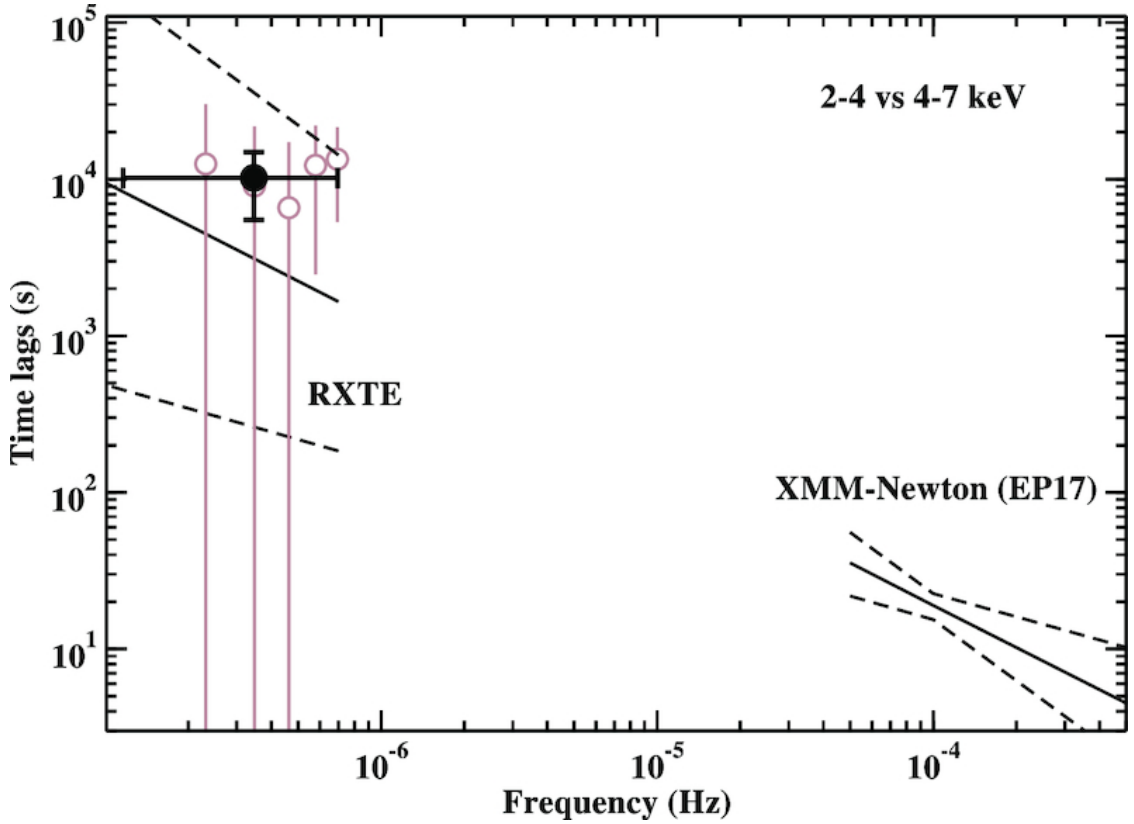


**Figure 1.5:** Empty circles show the time-lag estimates of NGC 4051 at low frequencies and the filled circle show their mean value. The solid continuous line shows the extrapolation of `EP17` model to low frequencies and the $1\sigma$ uncertainty (dashed lines) (figure taken from Papadakis et al., 2019).

# Chapter 2: Data analysis

We used 2–4, 4–7 and 7–10 keV light curves of 3 AGN observed with *Rossi X-ray Timing Explorer (RXTE)*. The light curves were obtained from the *RXTE AGN Timing & Spectral Database* (https://cass.ucsd.edu/∼ rxteagn/). We discuss briefly the data reduction details below. Our goal is to estimate the 2–4 vs 4–7 keV ("Soft-vs-Hard1" or "S-vs-H1", hereafter) and the 2–4 vs 7–10 keV ("Soft-vs-Hard2" or "S-vs-H2", hereafter) time-lags following the `EP16` method.

*The "RXTE AGN Timing & Spectral Database"*: This database provides uniformly analyzed light curves and spectra for all AGN observed by the *Rossi X-ray Timing Explorer (RXTE)* during its mission from Dec. 1995 to Jan. 2012. For each object in our sample, the database provides light curves flux in the sub-bands 2–4, 4–7 and 7–10 keV. We provide below some information regarding the data reduction and analysis of the *RXTE* data in this database.

Proportional Counter Array (PCA) spectra were extracted for each observation using `HEASOFT` version 6.7 and the "rex" perl script. PCA STANDARD-2 data were extracted from PCUs 0, 1 and 2 prior to 1998 December 23; PCUs 0 and 2 from 1998 December 23 until 2000 May 12; and PCU 2 only after 2000 May 12. Events from the top Xe layer only were used in order to maximize signal-to-noise. Standard screening was applied: data were rejected if taken within 20 minutes of the spacecraft's passing through the South Atlantic Anomaly (`TIME_SINCE_SAA`), if `ELECTRON0` $> 0.1$ (`ELECTRON2` for data after 2000 May 12), if the spacecraft was pointed within 10 degrees of the Earth, or if the source was $> 0.02$ degrees from the optical axis. All time-averaged spectral files were using the 2011 PCA background models "`pca_bkgd_cmvle_eMv20111129.mdl`" or "`pca_bkgd_cmfaintl7_eMv20111129.mdl`" for source fluxes brighter/fainter than $\sim 5$ mCrab, respectively.

Light curves are in flux units (i.e. $ergs^{-1}cm^{-2}$), with one data point per observation. The flux in each band was generated via a simple power-law fit to the spectrum in that band only. Mkn 766 was modeled by Rivers et al. (2013) with ionised absorption. Uncertainties on each flux point were obtained by dividing the standard deviation of the $N$ 16-s binned count rate light curve points in that observation by $\sqrt{N}$.

Since the cadence of RXTE observations of a source usually varies throughout its 16 years of operation, the light curves are not evenly sampled. However, the `EP16` method requires the use of evenly sampled light curves. We describe below the procedure we followed to create evenly sampled light curves for the three objects in our sample.

## 2.1 MCG-6–30–15

MCG-6–30–15 was observed by *RXTE* for almost 15 years, from March 1996 until December 2010 (50159.8–55559.8 MJD). However, the cadence of observations was highly inhomogeneous. Fig. (2.1) shows the light curve of MCG-6–30–15 as it has been observed by *RXTE*. The time difference between the observations ranges from a few hours to a month, while there are some even larger gaps without any observations. The longest is a year long gap from February 28th, 2006 until March 2nd, 2007 (53795.0–54161.9 MJD). Another long gap appears between 54525.536933–54797.672025 MJD (February 29th,

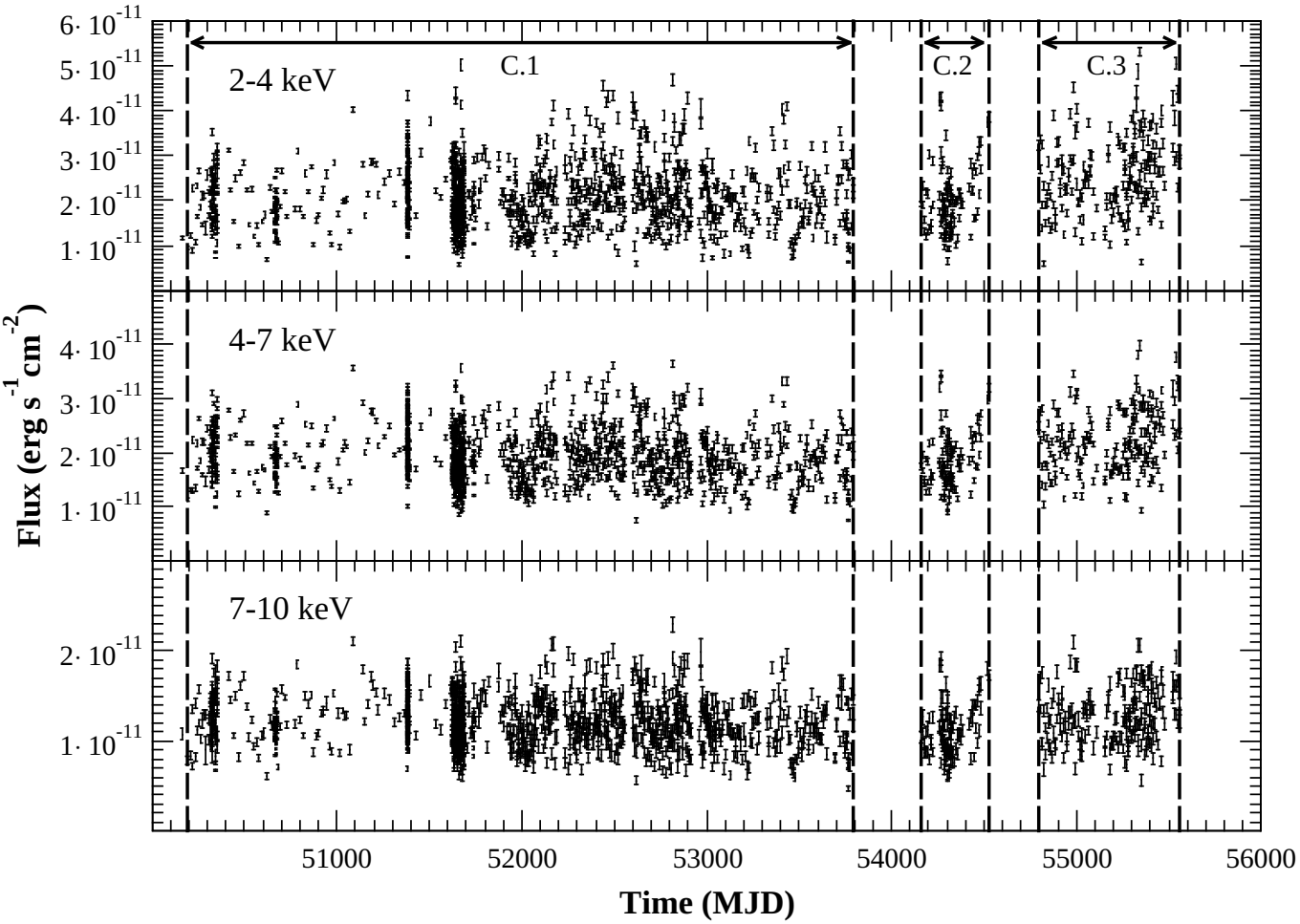


**Figure 2.1:** From top to bottom: The *RXTE* 2–4, 4–7 and 7–10keV light curves of MCG-6–30–15. Vertical lines indicate the start/stop time of the three parts of the light curve we consider as Group C.

2008–November 27th, 2008). Additionally, the source has only been observed 9 times over a period of 7.5 months, from early August 1999 until late March 2020. On the other hand, the source was observed hundred times over sort periods of time. As an example, the source was observed 95 times for a period of only 10 days before August 1999, once every 100 minutes, on average. Likewise, the source was observed 263 times with an average of 4 observations daily, for a period of about 2 months after March 19th, 2000 until May 24th, 2000. For the most part after January 21th, 2001 (51931.1 MJD), the source was observed every 2 or 4 days (excluding the two large gaps mentioned above).

In order to construct evenly sampled light curves first we identify light curve parts with similar time difference, $\Delta t_{j-i}$, between the observations. For these parts we measure their duration ($T$) and number of observations ($N_{obs}$). The ratio $T/N_{obs}$ gives an estimate of the average time difference between the observations. We search for light curve parts where $T/N_{obs}$ is roughly equal to $\Delta t_{j-i,\ median}$. The segments which satisfy this criterion should not contain any major gaps.

We identify 30 parts (segments) for which $T/N_{obs} \sim \Delta t_{j-i,\ median}$ in the MCG-6–30–15 light curve. These segments are listed on Table 2.1. The first column indicates the start/end time of each segments in MJD. The following columns list $N_{obs}$, $T$, $T/N_{obs}$ and $\Delta t_{j-i,\ median}$.

According to `EP16`, reliable estimates of the time-lags require the use of $\sim 20$ segments to compute the cross-periodogram, in order to bin the real and the imaginary part of the cross-periodograms. The segments should have the same duration and bin size, $\Delta t_{bin}$. For example, many segments in Table 2.1 have a median $\Delta t_{j-i,\ median} \simeq 2d$, with no major gaps in them. We could use them to compute the

**Table 2.1:** Segments in MCG-6–30–15 light curve

| | Time (MJD) | $N_{obs}$ | Duration (T) (days) | $T/N_{obs}$ (days) | $\Delta t_{j-i,\ median}$ (days) |
|---|---|---|---|---|---|
| 1 | 50159.77–50316.25 | 18 | 156.48 | 8.69 | 6.94 |
| 2 | 50318.30–50355.56 | 60 | 37.26 | 0.62 | 0.58 |
| 3 | 50411.92–50661.22 | 19 | 249.30 | 13.12 | 14.14 |
| 4 | 50664.27–50672.51 | 40 | 8.24 | 0.21 | 0.23 |
| 5 | 50679.70–51378.13 | 41 | 698 | 17.02 | 14.21 |
| 6 | 51378.13–51388.22 | 95 | 10.09 | 0.11 | 0.07 |
| 7 | 51394.77–51622.68 | 9 | 227.91 | 25.32 | 29.11 |
| 8 | 51622.68–51688.55 | 263 | 65.87 | 0.25 | 0.25 |
| 9 | 51688.55–51735.14 | 8 | 46.59 | 5.82 | 6.63 |
| 10 | 51735.14–51737.64 | 10 | 2.50 | 0.25 | 0.19 |
| 11 | 51738.14–51930.88 | 23 | 192.74 | 8.38 | 7.06 |
| 12 | 51931.11–52188.79 | 127 | 257.68 | 2.03 | 1.99 |
| 13 | 52231.11–52554.75 | 150 | 323.64 | 2.16 | 2.00 |
| 14 | 52601.19–52915.46 | 166 | 314.28 | 1.89 | 1.97 |
| 15 | 52961.98–53055.06 | 48 | 93.08 | 1.94 | 2.03 |
| 16 | 53061.10–53283.06 | 53 | 221.96 | 4.19 | 4.27 |
| 17 | 53326.90–53649.68 | 75 | 322.79 | 4.30 | 4.28 |
| 18 | 53692.67–53759.57 | 17 | 66.90 | 3.94 | 4.30 |
| 19 | 53759.57–53760.67 | 5 | 1.10 | 0.22 | 0.15 |
| 20 | 53765.08–53765.81 | 5 | 0.73 | 0.15 | 0.18 |
| 21 | 53765.81–53794.96 | 8 | 29.15 | 3.64 | 3.76 |
| 22 | 54161.88–54225.98 | 16 | 64.10 | 4.01 | 4.26 |
| 23 | 54259.16–54329.13 | 65 | 69.97 | 1.08 | 0.98 |
| 24 | 54329.13–54380.98 | 14 | 51.85 | 3.99 | 4.03 |
| 25 | 54422.87–54485.84 | 17 | 62.96 | 3.70 | 3.94 |
| 26 | 54797.67–55109.53 | 74 | 311.85 | 4.21 | 3.99 |
| 27 | 55153.98–55249.73 | 24 | 95.74 | 3.99 | 3.99 |
| 28 | 55253.72–55423.25 | 83 | 169.53 | 2.04 | 1.97 |
| 29 | 55423.25–55475.94 | 14 | 52.69 | 3.76 | 4.02 |
| 30 | 55519.73–55559.80 | 11 | 40.07 | 3.64 | 4.11 |

time-lags at frequencies lower than $1/(2 \cdot 2d) \simeq 3 \times 10^{-6} Hz$. However, they are unevenly sampled and their number is considerably smaller than 20. We explain below how we can use them to calculate the time-lags.

### 2.1.1 Light curve parts with $\Delta t_{bin} \sim 2d$

The segments with $\Delta t_{j-i,\ median} \simeq 2d$ are listed in Table 2.2, under the label "Group A". First, we divide them into parts with duration $T_s \sim 62d$. In this way we ended up with 19 segments with the same duration. We can use these segments to estimate the time-lags from $3 \times 10^{-6} Hz$ down to $1/T_s \simeq 2 \times 10^{-7} Hz$. However, the data points in these segments are not equidistant. We used the observed segments to create evenly sampled segments with a bin size of $\Delta t_{bin}$, as follows.

We started with the first point in each segment and we computed 2–4, 4–7 and 7–10 keV flux

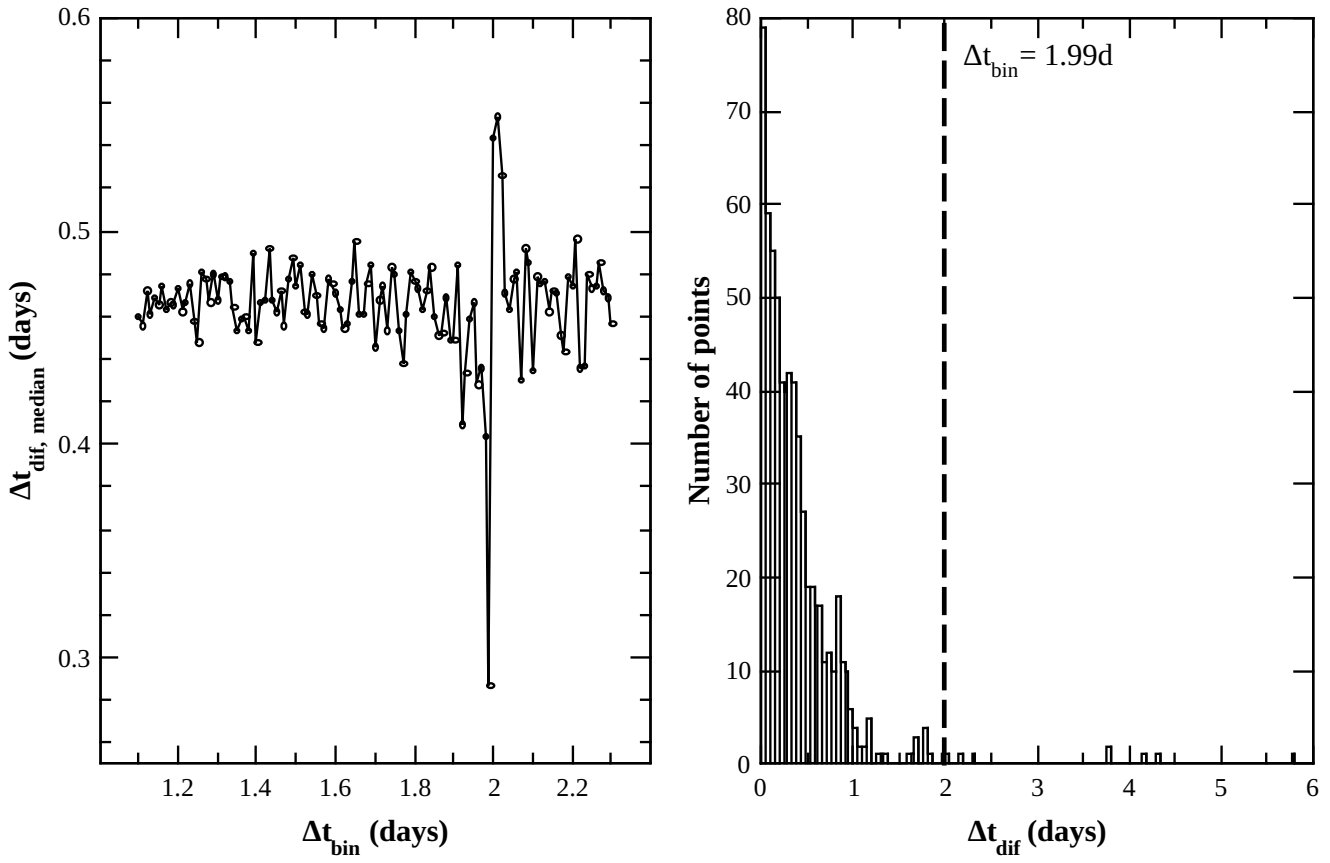


**Figure 2.2:** (Left panel): $\Delta t_{dif,\ median}$ plotted as a function of $\Delta t_{bin}$ for segments in Group A. (Right panel): Histogram of $\Delta t_{dif}$ for $\Delta t_{bin} = 1.99d$ (indicated by the vertical line).

estimates, $f_i$, at points $i\Delta t_{bin}$ with $i = 1, 2, \ldots, N_{obs}^{s}$ [1] using linear interpolation between the observed flux measurements, $f_{obs}$, at time just before and just after $i\Delta t_{bin}$. The linear interpolation procedure is described in detail in Appendix A.

In order to choose the best $\Delta t_{bin}$, we created equidistant time points, $i\Delta t_{bin}$, using different values of $\Delta t_{bin}$ from $\Delta t_{bin} = 1.1d$ up to $\Delta t_{bin} = 2.3d$, with a time step of $0.01d$. For each time step we computed the time difference, $\Delta t_{dif}$, between $i\Delta t_{bin}$ and the time of the closest observational data point. Then, we compute the mean and the median $\Delta t_{dif}$ for all $\Delta t_{bin}$. The median time difference, $\Delta t_{dif,\ median}$, for each bin size is plotted in the left panel of Fig. (2.2). For most values of $\Delta t_{bin}$, $\Delta t_{dif,\ median} \simeq 0.47d$. The smallest $\Delta t_{dif,\ median} = 0.29d$ and appears for $\Delta t_{bin} = 1.99$. If we adopt this bin size we will be able to produce evenly sampled light curves with data points closer to the time of actual observations. The right panel of Fig. (2.2) shows a histogram of $\Delta t_{dif}$ for $\Delta t_{bin} = 1.99d$. $\Delta t_{dif}$ is smaller than a day (half of the bin size) for 95% of the interpolated data points. The maximum $\Delta t_{dif}$ is $5.76d$ and occurs in a $\sim 11d$ gap inside segment 13. In this gap we have included 6 interpolated points. In the second largest gap, 5 interpolated points have been added and the maximum $\Delta t_{dif}$ of these points is $4.30d$. In the rest of the the light curve segments no more than three consecutive interpolated points appear. Table 2.2 lists the mean and median value of $\Delta t_{dif}$ along with other useful calculations for the accepted bin size.

**Table 2.2:** Groups of segments we used to compute the time-lags of MCG-6–30-15.

| **Segments** | $N/N_{obs}$ | $\overline{\Delta t_{dif}}$ (days) | $\sigma_{\Delta t_{dif}}$ (days) | $\Delta t_{dif,\ median}$ (days) | % $\Delta t_{bin}/4$ | % $\Delta t_{bin}/2$ |
|---|---|---|---|---|---|---|
| **Group A** ($\Delta t_{bin} = 1.99d$, $n_s = 19$, $T_s = 61.69d$, $N_s^{obs} = 32$) | | | | | | |
| 8 | 34/263 | | | | | |
| 12 | 130/127 | | | | | |
| 13 | 163/150 | | | | | |
| 14 | 158/166 | 0.40 | 0.50 | 0.29 | 72.63 | 94.34 |
| 15 | 47/48 | | | | | |
| 23 | 35/65 | | | | | |
| 28 | 85/83 | | | | | |
| **Group B** ($\Delta t_{bin} = 3.98d$, $n_s = 15$, $T_s = 119.4d$, $N_s^{obs} = 31$) | | | | | | |
| 12 | 65/127 | | | | | |
| 13 | 82/150 | | | | | |
| 14 | 79/166 | | | | | |
| 15 + 16 | 81/102 | 0.67 | 0.72 | 0.46 | 78.62 | 96.2 |
| 17 | 82/75 | | | | | |
| 23 + 24 | 31/78 | | | | | |
| 26 | 79/74 | | | | | |
| 27 + 28 + 29 | 81/120 | | | | | |
| **Group C** ($\Delta t_{bin} = 12.8d$, $n_s = 18$, $T_s = 243.2d$, $N_s^{obs} = 20$) | | | | | | |
| C.1 | 282/1236 | | | | | |
| C.2 | 29/113 | 3.07 | 4.80 | 0.90 | 75.20 | 84.91 |
| C.3 | 60/204 | | | | | |

### 2.1.2 Light curve parts with $\Delta t_{bin} \sim 4d$

For the most part after February 25, 2004 (53061.1 MJD), the source was observed every $\sim 4$ days (i.e. $\Delta t_{j-i,\ median} \simeq 4d$). We can use those segments to compute the time-lags at frequencies $< 1/(2 \times 4d) \simeq 1.5 \times 10^{-6} Hz$. However, the number of segments with a value of $\Delta t_{j-i,\ median} \sim 4d$ is significantly smaller than 20. If we further divide the segments into smaller parts, those parts will be short in duration and this will limit the lower frequency that we can estimate the time-lags. To increase the number of segments and have a better range of frequencies, we will also use segments with $\Delta t_{j-i,\ median} \sim 1d$ and $2d$ in addition to those with $\Delta t_{j-i,\ median} \sim 4d$. Those segments are labeled in Table 2.2 as "Group B".

We divide those segments into smaller parts with duration $T_s = 120d$. Segments (15 + 16), (23 + 24) and (27 + 28 + 29) are consecutive segments with different $\Delta t_{j-i,\ median}$ and do not contain any major gaps in between. We consider those segments as one, and then we divided them into smaller segments with 120 days duration. We end up with 15 segments with $N_s^{obs} = 31$ using the Group B light curve parts.

Similarly with Group A, we search which bin size produces points closer to the actual observations. We measure $\Delta t_{dif,\ median}$ for $\Delta t_{bin} = 3.5d$–$4.6d$, with a time step of $0.02d$ as shown in the left panel in Fig. (2.3). $\Delta t_{dif,\ median} \simeq 0.66d$ for most $\Delta t_{bin}$ values. But $\Delta t_{dif,\ median} = 0.46d$ resulted as the lowest value at $\Delta t_{bin} = 3.98d$.

We therefore chose $\Delta t_{bin} = 3.98d$. Starting from the first point in each segment, we linearly

[1] $N_{obs}^s$ is the number of observation in each 62 days long segment.

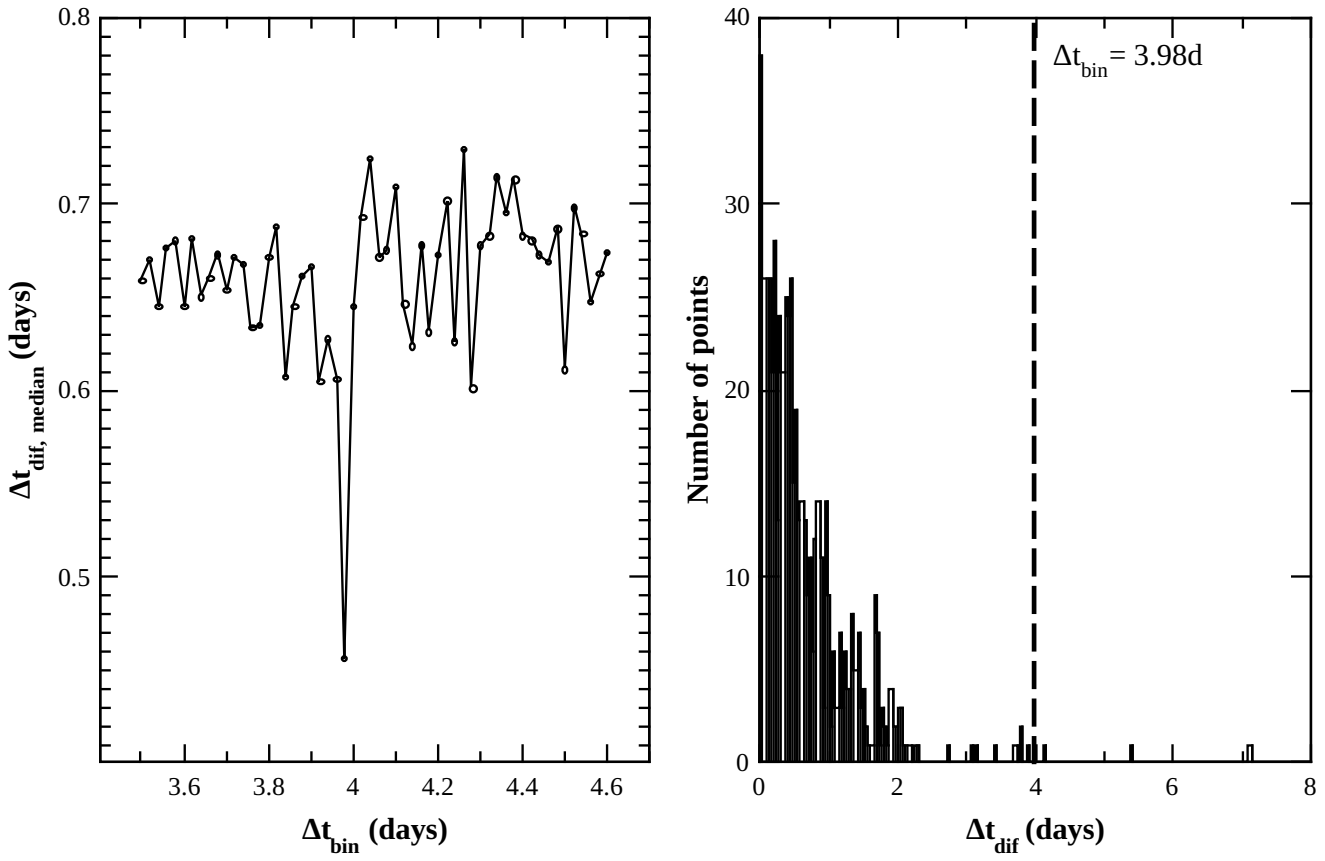


**Figure 2.3:** (Left panel): $\Delta t_{dif,\ median}$ plotted as a function of $\Delta t_{bin}$ for segments in Group B. (Right panel): Histogram of $\Delta t_{dif}$ for $\Delta t_{bin} = 3.98d$ (indicated by the vertical line).

interpolate to produce evenly sampled segments. We used these segments and we computed the time-lags at frequencies from $1/T_s = 9.6 \times 10^{-8} Hz$ to $1/(2\Delta t_{bin}) = 1.5 \times 10^{-6} Hz$. For $\Delta t_{dif} = 3.98d$, $\Delta t_{dif}$ is smaller than 2 days for 96% of the interpolated data points (see right panel of Fig. (2.3)). The maximum $\Delta t_{dif}$ is $7.13d$ and we have added no more than 4 continuous interpolated points between two observational data points in any of the segments we used.

### 2.1.3 Light curve parts with $\Delta t_{bin} > 10d$

Finally, we tried to identify light curve parts which are long, so that we can estimate the time-lags at the lowest possible frequencies. To avoid heavy interpolation, we require these segments not to be separated by very large gaps. Segments C.1, C.2 and C.3, indicated by the the horizontal arrows in Fig. (2.1), satisfy these criteria and consist "Group C". C.1 is the first part of the light curve between 50160–53795 MJD, which include segments 1–21. It is the longest part in group C and includes 1236 observations in total, spread over a period of about 10 years. The median of the time difference between observations in this light curve part is $\Delta t_{j-i,\ median} = 1.80d$. The second segment, C.2, begins at 54162MJD and its duration is about 364 days, until 54526MJD. It contains 113 observations with $\Delta t_{j-i,\ median} = 1.57d$. C.3 starts at 54798MJD and is extended until the end at 55560MJD, containing 204 observations over a period of about 2 years ($\Delta t_{j-i,\ median} = 3.73d$).

We compute $\Delta t_{dif,\ median}$ for different values of $\Delta t_{bin}$ between 11 and 15 days, with a time step of $0.1d$. The left panel of Fig. (2.4) shows the median value of the time difference for each bin size, $\Delta t_{bin}$. $\Delta t_{dif,\ median} \sim 1.2d$ on average and the lowest value $\Delta t_{dif,\ median} = 0.9d$ resulted for $\Delta t_{bin} = 12.8d$. We

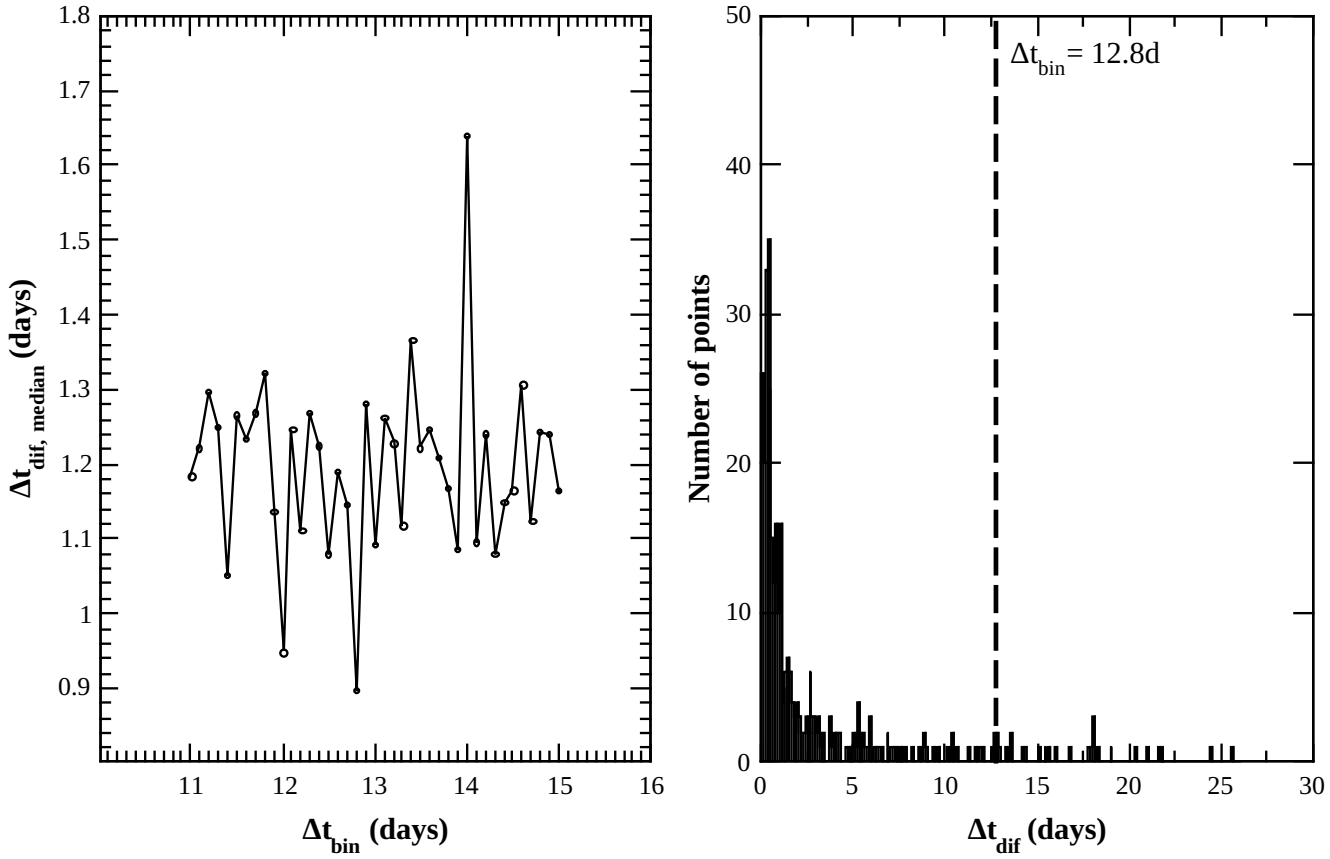


**Figure 2.4:** (Left panel): $\Delta t_{dif,\ median}$ plotted as a function of $\Delta t_{bin}$ for segments in Group C. (Right panel): histogram of $\Delta t_{dif}$ for $\Delta t_{bin} = 12.8d$ (indicated by the vertical line).

therefore choose $\Delta t_{bin} = 12.8d$, and we created $T_s = 243.2d$ long segments to measure the time-lag from $1/T_s = 4.8 \times 10^{-8} Hz$ up to $1/(2\Delta t_{bin}) = 4.5 \times 10^{-7} Hz$. We end up with 18 segments ($n_s = 18$), with 20 points in each segment ($N_s^{obs} = 20$) as shown in Table 2.2, under the label "Group C".

In the right panel of Fig. (2.4) we show a histogram of the time difference, $\Delta t_{dif}$, for $\Delta t_{bin} = 12.8d$. $\Delta t_{dif}$ is smaller than 6 days (i.e. half of the bin size) for 85% of the interpolated data points and 6 point have $\Delta t_{dif} > 20d$. Inside the largest gap we have 5 continuous interpolated points and no more than 3 consecutive interpolated points appear in the rest of the light curve.

## 2.2 Ark 564

The *RXTE* observations of Ark 564 started on December 23, 1996. However there are only 5 observations between December 23–24, 1996, and a long (∼2 years) gap follows until January 1st, 1999. Then, the source was observed once every 4–5 days for most of the time, without any major gaps, until March 4th, 2003. During the 10 month period from January 1st 1999 to October 28th, 1999, the source was observed 71 times, once every 4–4.5 days on average. Similarly, from November 12, 1999 until May 30th, 2000 Ark 564 was observed 44 times over a period of almost 200 days with the same cadence of observation. The last and the longest part of the light curve begins on July 4th, 2000 and ends on March 4th, 2003. It contains 211 observations over a period of 2 years and 8.5 months with an average of 4.5 observations daily. The source was observed more frequently over two short periods of time. 19 times (i.e. twice a day) from October 28 to November 8, 1999, and 219 times from May 30 to June 30,

2020 (i.e. once every 3–3.5 hours). The light curve of Ark 564 is plotted in Fig. (2.5).

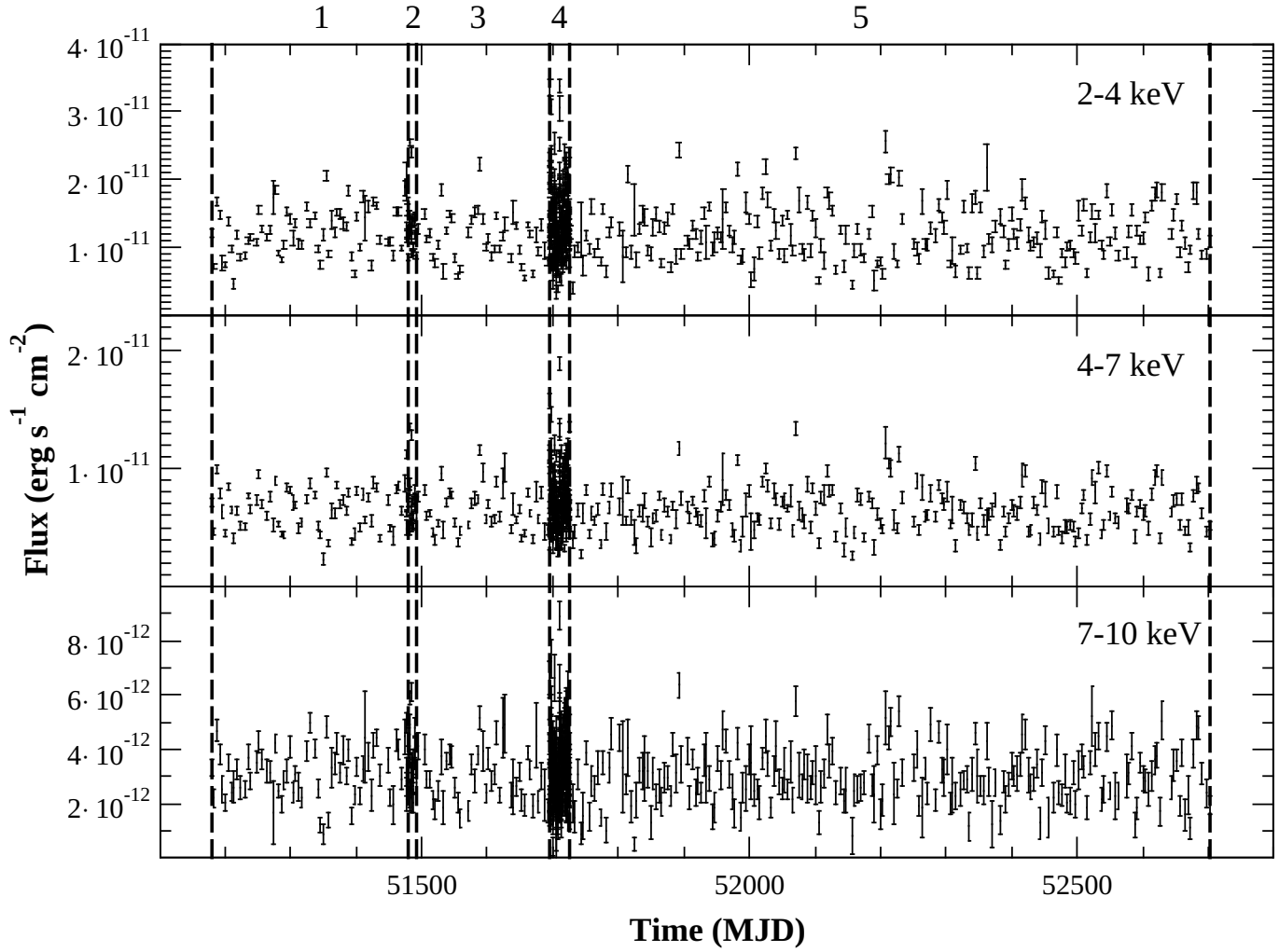


**Figure 2.5:** From top to bottom: The *RXTE* 2–4, 4–7 and 7–10keV light curves of Ark 564. Vertical lines indicate the start/stop time of the light curve parts we identified in Table 2.3.

As we did for MCG-6–30–15, we search for segments with similar $\Delta t_{j-i}$ between observations. The light curve parts we discuss above have a ratio $T/N_{obs}$ roughly equal to $\Delta t_{j-i,\ median}$ and do not contain any major gaps inside and in between the segments. We ignore the first few observations on December 23/24, 1996. The remaining 5 segments for which $T/N_{obs} \sim \Delta t_{j-i,\ median}$ are listed on Table 2.3. The first column indicates the borders of the segments in MJD and the following columns list $N_{obs}$, $T$, $T/N_{obs}$ and $\Delta t_{j-i,\ median}$.

**Table 2.3:** Segments in Ark 564 light curve

| | Time (MJD) | $N_{obs}$ | Duration (T) (days) | $T/N_{obs}$ (days) | $\Delta t_{j-i,\ median}$ (days) |
|---|---|---|---|---|---|
| 1 | 51179.55–51479.78 | 71 | 300.23 | 4.23 | 4.265 |
| 2 | 51480.38–51491.03 | 19 | 10.65 | 0.56 | 0.543 |
| 3 | 51495.41–51694.83 | 44 | 199.42 | 4.53 | 4.26 |
| 4 | 51695.05–51726.46 | 219 | 31.412 | 0.14 | 0.137 |
| 5 | 51729.93–52702.85 | 211 | 972.923519 | 4.61 | 4.28 |

### 2.2.1 Light curve parts in Ark 564 light curve

We will consider two groups of segments. The are listed in Table 2.4 under the label "Group A" and "Group B" respectively. First group include all light curve parts listed in Table 2.3, while group B consists of the 4th light curve part only, which we will use to estimate time-lags at high frequencies.

We divide the first group into segments with duration $T_s \approx 68d$ and we end up with 21 segments to measure the time-lags at frequencies $> 1/T_s = 1.7 \times 10^{-7} Hz$. Like in MCG-6–30–15, we search which bin size results in points closer to the actual observations, starting from $\Delta t_{bin} = 4.2d$ up to $4.8d$ with a time step of 0.01 days. The left panel of Fig. (2.6) shows the median time difference of the interpolated points and observations for the different values of $\Delta t_{bin}$. For the most $\Delta t_{bin}$ values, $1d < \Delta t_{dif,\ median} < 1.2d$. However, for $\Delta t_{bin} = 4.27d$ the median time difference is significantly lower ($\Delta t_{dif,\ median} = 0.66d$). We therefore choose this value for the bin size to measure time-lags at frequencies up to $1/(2 \times 4.27d) = 1.4 \times 10^{-6} Hz$. In the right panel of Fig. (2.6) we show a histogram of the time difference for $\Delta t_{bin} = 4.27d$. $\Delta t_{dif}$ is smaller than 2 days for 92% of the interpolated data points. The largest gap is $7.87d$ long, and we have added 4 consecutive interpolated points. In the rest of the light curve there are maximum 3 consecutive interpolated points between two observations.

During light curve part 4 in Table 2.3, the source was observed 219 times over a period of one month from May 30 until June 30, 2000. We divide this light curve part into 17 segments, with duration 1.703 days to measure time-lags at frequencies $> 1/1.703d = 6.8 \times 10^{-6} Hz$. We need to produce equidistance light curve points thus, as before, we search which bin size produces points closer to the actual observations. We measure $\Delta t_{dif,\ median}$ for different values of $\Delta t_{bin}$ from 0.08 days up to 0.2 days with a time step of 0.001d. In the right panel of Fig. (2.7) we show the results of the median time difference for the different $\Delta t_{bin}$. In most cases, the median time difference is $\sim 0.036d$. The lowest value ($\Delta t_{dif,\ median} = 0.027d$) appears for $\Delta t_{bin} = 0.131d$. We choose this value for the bin size to measure time lags from frequencies $8 \times 10^{-6}$ up to $1/(2 \times 0.131d) = 4.4 \times 10^{-5} Hz$.

A histogram of the time difference, $\Delta t_{dif}$, for the bin size we choose is shown in the right panel of Fig. (2.7). 88% of the interpolated data points have a value $< 0.065d$ (approximately $\Delta t_{bin}/2$). Only 3 interpolated data point have a time difference greater than the bin size (i.e. $> 0.131d$). The longest is 0.188d (i.e. $1.44\Delta t_{bin}$) followed by 0.165d. These appear on two short gaps of 0.406d and 0.402d. In these gaps we have added 3 interpolated points between the observations. The third longest time difference is 0.154d and is not much larger than the bin size. In this gap as well as in the rest of the light curve no extra points have been added between the observations (i.e. there is one interpolated point between two consecutive observations).

**Table 2.4:** Groups of segments we used to compute the time-lags of Ark 564.

| **Segments** | $N/N_{obs}$ | $\overline{\Delta t_{dif}}$ (days) | $\sigma_{\Delta t_{dif}}$ (days) | $\Delta t_{dif,\ median}$ (days) | % $\Delta t_{bin}/4$ | % $\Delta t_{bin}/2$ |
|---|---|---|---|---|---|---|
| **Group A** ($\Delta t_{bin} = 4.27d$, $n_s = 21$, $T_s = 68.32d$, $N_s^{obs} = 17$) | | | | | | |
| 1-5 | 357/564 | 0.87 | 1.04 | 0.66 | 82.63 | 91.88 |
| **Group B** ($\Delta t_{bin} = 0.131d$, $n_s = 17$, $T_s = 1.703d$, $N_s^{obs} = 14$) | | | | | | |
| 4 | 240/219 | 0.036 | 0.031 | 0.027 | 56.67 | 87.92 |

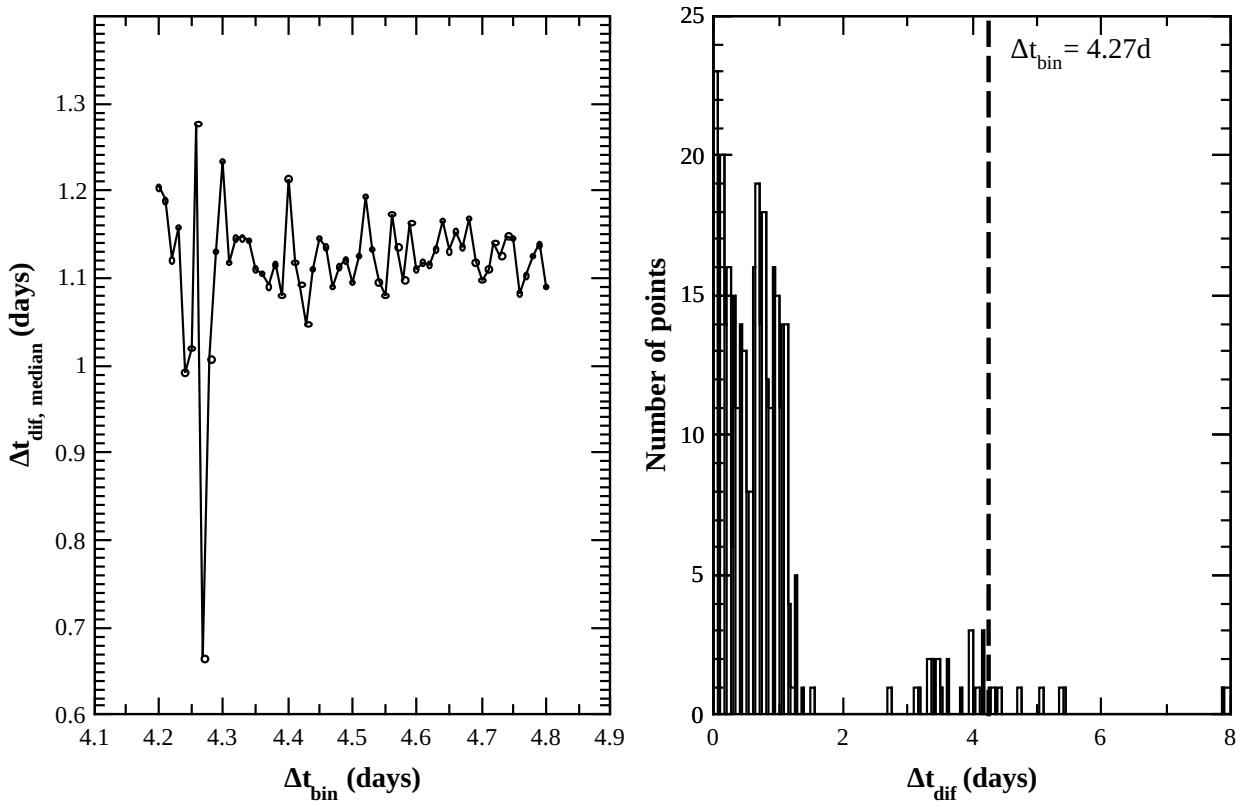


**Figure 2.6:** (Left panel): $\Delta t_{dif,\ median}$ plotted as a function of $\Delta t_{bin}$ for Group A segments of Ark 564. (Right panel): Histogram of $\Delta t_{dif}$ for $\Delta t_{bin} = 4.27d$ (indicated by the vertical line).

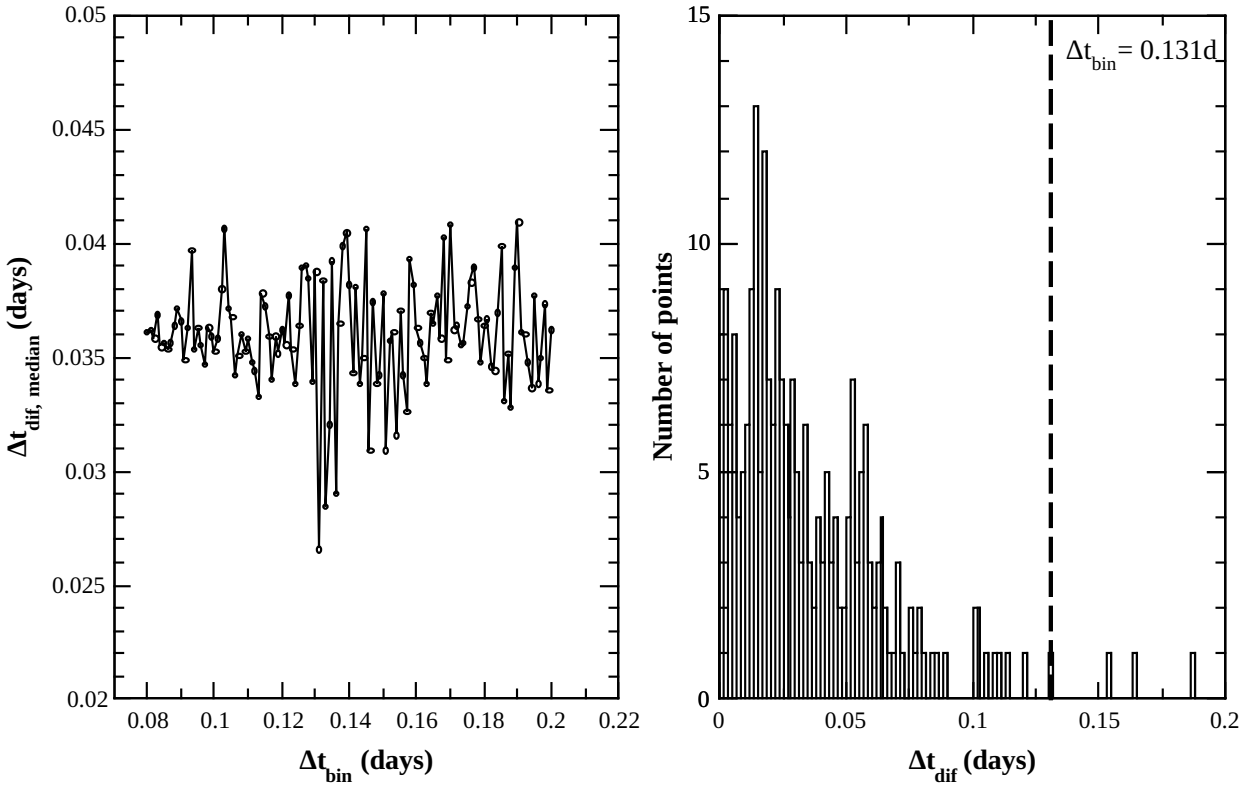


**Figure 2.7:** (Left panel): $\Delta t_{dif,\ median}$ plotted as a function of $\Delta t_{bin}$ for Group B segments of Ark 564. (Right panel): Histogram of $\Delta t_{dif}$ for $\Delta t_{bin} = 0.131d$ (indicated by the vertical line).

## 2.3 Mkn 766

Mkn 766 was first observed by RXTE for 5 days between May 4th and May 10th, 2001. Then, a large 2 year and about 10 month gap follows and observations resumed on February 19th, 2004. The source was then observed regularly, once every 4–4.5 days for the most part until December 28, 2011. Fig. (2.8) shows the 2–4keV, 4–7keV and 7–10keV light curves of Mkn 766 as it has been observed by RXTE. After February 19th, 2004, month-long gaps appear throughout the light curve. The longest gap occurs after September 3rd until October 4, 2009. Additionally, there are 4 gaps which are $\sim$ 25–26 days long and 3 gaps which are $\sim$ 21.5 days long. Excluding those gaps, the rest of the light curve do not contain any major gaps and the longest difference between two consecutive observation is less than 8.8 days.

For the most part of the light curve the cadence of observation is $\sim$ 4–4.5 days. In total the source was observed 618 times between February 29, 2004 and December 28, 2011 (including gaps), once every 4–4.5 days. Additionally, there are two short period when the source was observed more frequently. Between May 22 and June 4, 2005, the source was observed 10 times over a period of about 13 days (i.e. once every 30 hours), and from November 28th, 2006 until January 1st, 2007 the source was observed 130 time in total, once every 6 hours, on average.

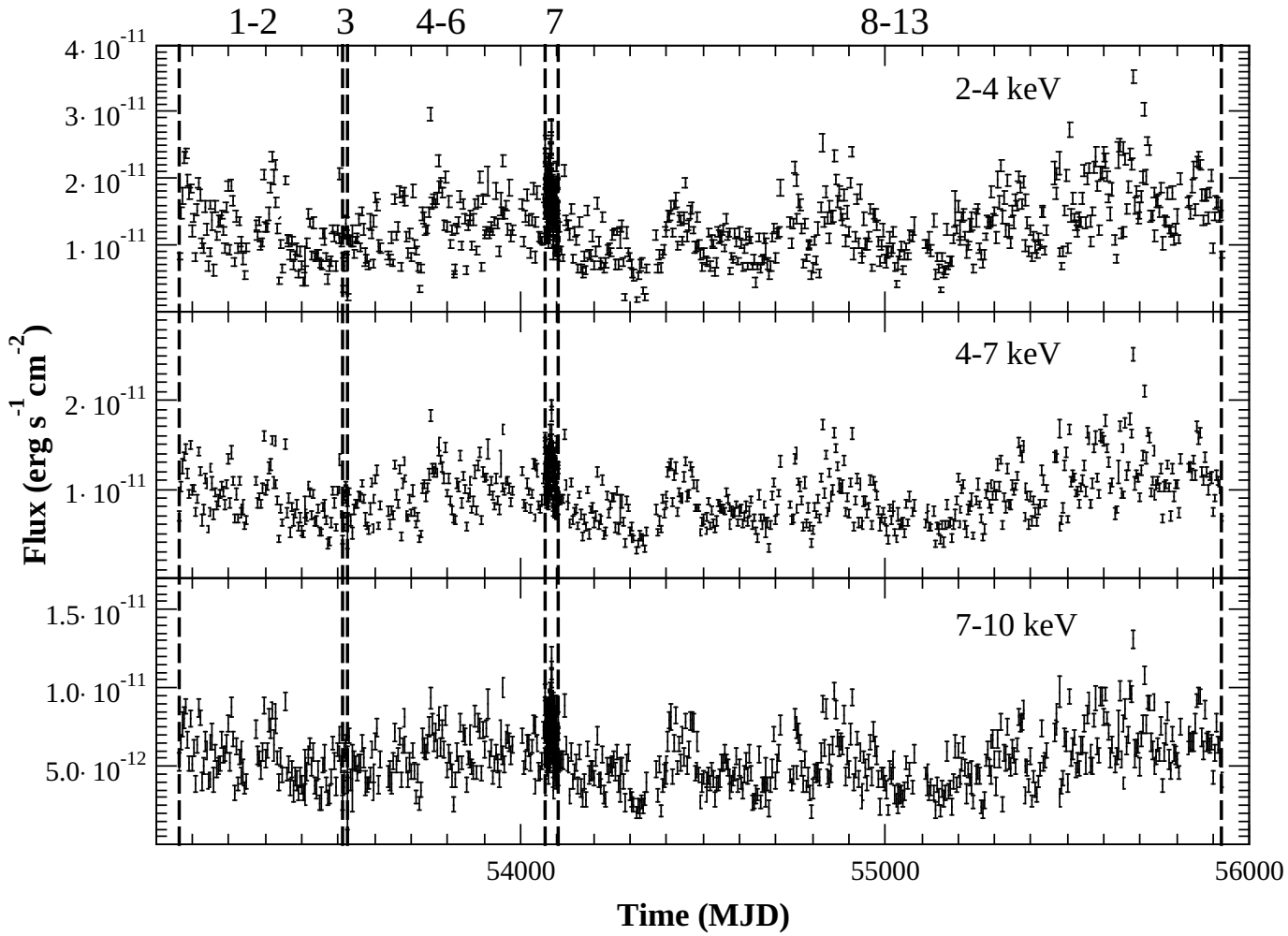


**Figure 2.8:** From top to bottom: the RXTE 2–4keV, 4–7keV and 7–10keV band light curves of Mkn 766. Vertical lines indicate the start/stop time of the light curve parts we identified in Table 2.5.

**Table 2.5:** Segments in Mkn 766 light curve.

| | Time (MJD) | $N_{obs}$ | Duration (T) (days) | $T/N_{obs}$ (days) | $\Delta t_{j-i,\ median}$ (days) |
|---|---|---|---|---|---|
| 1 | 53065.44–53248.80 | 44 | 183.37 | 4.17 | 4.262 |
| 2 | 53274.52–53514.44 | 56 | 238.92 | 4.27 | 4.267 |
| 3 | 53513.44–53526.22 | 10 | 12.78 | 1.278 | 1.234 |
| 4 | 53526.22–53615.63 | 22 | 89.41 | 4.06 | 4.279 |
| 5 | 53637.12–53978.40 | 81 | 341.28 | 4.21 | 4.266 |
| 6 | 54003.74–54068.06 | 16 | 64.32 | 4.02 | 4.190 |
| 7 | 54068.06–54102.49 | 130 | 34.42 | 0.26 | 0.262 |
| 8 | 54102.49–54345.68 | 57 | 243.20 | 4.27 | 4.230 |
| 9 | 54371.15–54712.37 | 81 | 341.22 | 4.21 | 4.268 |
| 10 | 54738.00–55078.37 | 80 | 340.37 | 4.25 | 4.251 |
| 11 | 55109.05–55441.76 | 77 | 332.71 | 4.32 | 4.238 |
| 12 | 55463.46–55808.96 | 81 | 345.50 | 4.27 | 4.249 |
| 13 | 55830.45–55924.11 | 23 | 93.66 | 4.07 | 4.250 |

As with the previous two sources, we search for light curve parts with $\Delta t_{j-i,\ median} \approx T_s/N_{obs}$, that do not include any major gaps in them. We ignore the first part between May 4th and May 10th, 2001. We have identified 13 parts/segments, which are listed on Table 2.5. The first column presents the start/stop time of each segment and the following columns list $N_{obs}$, $T$, $T/N_{obs}$ and $\Delta t_{j-i,\ median}$. In the following subsection we discuss how we used these segments to estimate the 2–4 vs 4–7 keV and 2–4 vs 7–10 keV time-lags for Mkn 766.

### 2.3.1 Light curve parts with $\Delta t_{bin} \sim 4d$

We can use all light curve parts in the Mkn 766 light curves to estimate the time-lags at low and high frequencies. Most of the light curve parts with $\Delta t_{dif,\ median} \simeq 4$–$4.5d$, are longer than 180 days, except light curve parts 4, 6 and 13, which are less than $\sim 90d$ long. We can still use these light curve parts together with neighboring parts as long as there not any major gaps in between. Thus, we will use light curve part 3, which has a higher cadence of observation of $\sim 1d$, together with segment light curve parts 2 and 4. And light curve part 7, which has a cadence of about 6 hour, with light curve parts 6 and 8. Light curve part 13, the last available part, has 23 observations over a period of about 3 months. There is a $\sim 20d$ long gap between the end of light curve part 12 and the start of part 13 and for this reason, we did not keep light curve part 13. The usable observations we consider to measure time-lags are listed in Table 2.6.

We end up with 8 light curve parts which are suitable for time-lag estimation. As before we need to produce evenly sampled light curves for the time-lag estimation. To do that we linearly interpolate and we test which value of $\Delta t_{bin}$ produces points closer to observations. To choose the value of the bin size, we test different values from 4 days up to 4.5 days with a time step of 0.01d. Fig. (2.9) (left panel) shows a plot of the median time difference between interpolated points and observations as a function of $\Delta t_{bin}$. The mean value of $\Delta t_{dif,\ median}$ is 1d and drops to 0.19d when $\Delta t_{bin} \sim 4.27d$. Therefore, we choose this value for the bin size to measure time-lags at frequencies $\leq 1/(2 \times 4.27d) = 10^{-6} Hz$.

We "chop" the 8 light curve parts of Table 2.6 intro shorter segments with duration $T_s \approx 110d$. In this way, we have 22 available segments to measure time-lags at frequencies $10^{-6} Hz \geq \nu \geq 1/111.02d \simeq 10^{-7} Hz$. 98.67% of the interpolated points differ less than a day from observations. Only one point have

**Table 2.6:** Groups of segments we used to compute the time-lags of Mkn 766.

| **Segments** | $N/N_{obs}$ | $\overline{\Delta t_{dif}}$ (days) | $\sigma_{\Delta t_{dif}}$ (days) | $\Delta t_{dif,\ median}$ (days) | % $\Delta t_{bin}/4$ | % $\Delta t_{bin}/2$ |
|---|---|---|---|---|---|---|
| **Group** ($\Delta t_{bin} = 4.27d$, $n_s = 22$, $T_s = 111.02d$, $N_s^{obs} = 27$) | | | | | | |
| 1 | 43/44 | | | | | |
| 2 + 3 + 4 | 80/86 | | | | | |
| 5 | 80/81 | | | | | |
| 6 + 7 + 8 | 81/201 | 0.26 | 0.42 | 0.19 | 98.88 | 98.88 |
| 9 | 80/81 | | | | | |
| 10 | 80/80 | | | | | |
| 11 | 78/77 | | | | | |
| 12 | 81/81 | | | | | |

a time difference $> \Delta t_{bin}$ and no more than 3 consecutive points have been added between observations. The right panel of Fig. (2.9) shows a histogram of the time difference between interpolated points and observations. The bin size in indicated by the vertical line on the plot.

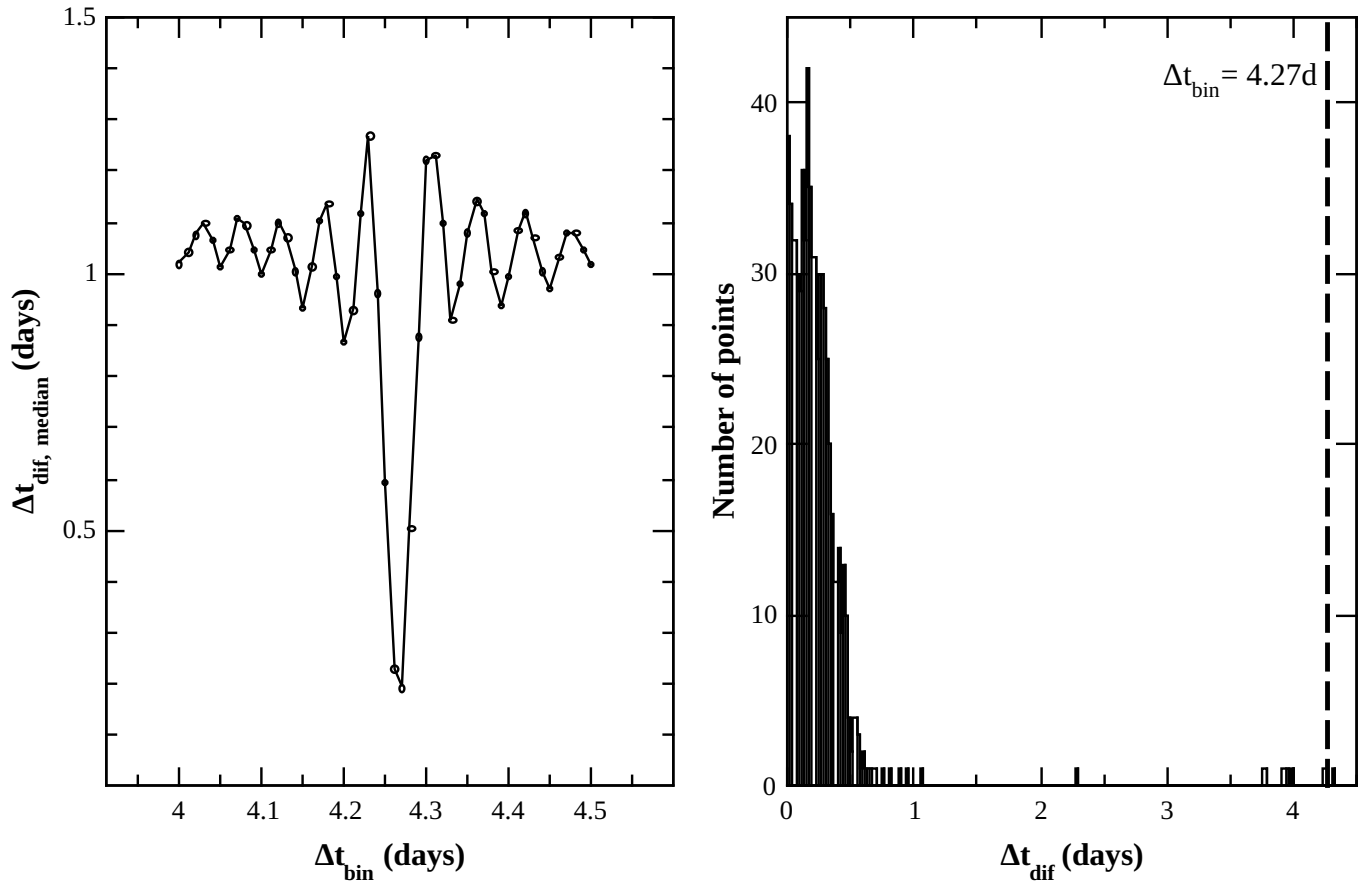


**Figure 2.9:** (Left panel): $\Delta t_{dif,\ median}$ plotted as a function of $\Delta t_{bin}$ for the group of segments of Mkn 766. (Right panel): Histogram of $\Delta t_{dif}$ for $\Delta t_{bin} = 4.27d$ (indicated by the vertical line).

# Chapter 3: Definitions and time-lag estimation

## 3.1 Definitions

Our main objective is to study the correlation between the observed variations in different energy bands of MCG–6-30-15, Ark 564 and Mkn 766. Study of the correlation between time variable quantities can be done either in the time or in the frequency domain. A delay in the time domain maps to a phase shift in the frequency domain. X-ray time series analysis to measure time-lags is done in the frequency domain by measuring the shift between the sinusoidal components of light curves at different energy bands. In this Chapter, first we will introduce the concept and tools we used to estimate the time-lags spectrum in the frequency domain and then we present our results in Sections 3.3–3.5.

Let us consider two time series $x(t)$, $y(t)$ with mean value $\bar{x}$ and $\bar{y}$, respectively. The function which is often used to qualify the corelation between two time series is the cross-covariance function (CCF), which is defined as follows

$$R_{xy}(\tau) \equiv E[(x(t) - \bar{x})(y(t+\tau) - \bar{y})], \tag{3.1}$$

where $E$ is the expectation operator, which gives the expected mean value or a random quantity, and $\tau$ is the so-called lag. A positive/negative value of $R_{xy}(\tau)$ at $\tau$ shows that $x(t)$ and $y(t)$ are positively correlated/anticorrelated with $x(t)$ leading $y(t)$. For stationary processes CCF depends only on $\tau$ and does not vary over time. The Fourier transformation of the CCF defines the cross-spectrum (CS),

$$h_{xy}(\nu) = \int_{-\infty}^{\infty} R_{xy}(\tau) e^{-i2\pi\nu\tau} d\tau. \tag{3.2}$$

Since $R_{xy}(\tau)$ is not necessarily symmetric at $\tau = 0$, the cross-spectrum is a complex number. Hence, it can be written as

$$h_{xy}(\nu) = \Re[h_{xy}(\nu)] - i\Im[h_{xy}(\nu)] = |h_{xy}(\nu)| e^{-i\phi_{xy}(\nu)} \tag{3.3}$$

where $\Re[h_{xy}(\nu)]$ and $\Im[h_{xy}(\nu)]$ are the real and imaginary parts of the cross-spectrum, $\phi_{xy}(\nu)$ is the phase lag and $|h_{xy}(\nu)|$ is the amplitude of the cross-spectrum. The phase-lag, $\phi_{xy}(\nu)$, can be defined as

$$\phi_{xy}(\nu) = \arctan\left[-\frac{\Im[h_{xy}(\nu)]}{\Re[h_{xy}(\nu)]}\right] = \arg[h_{xy}(\nu)], \tag{3.4}$$

and it gives the average phase shift between the two Fourier components of the time-series at frequency $\nu$. The phase-lag can be transformed into the corresponding time-lag as follows,

$$\tau_{xy}(\nu) = \frac{\phi_{xy}(\nu)}{2\pi\nu}. \tag{3.5}$$

$\tau_{xy}(\nu)$ as a function of frequency, defines the time-lag spectrum and represents the average time delay between sinusoidal components of the two time-series with frequency $\nu$.

Another statistical parameter that is often used to study correlations between two random processes in Fourier space is the so-called coherence function

$$\gamma^2_{xy}(\nu) = \frac{|h_{xy}(\nu)|^2}{h_x(\nu)h_y(\nu)}, \tag{3.6}$$

where $h_x(\nu)$ and $h_y(\nu)$ denote the power spectral density (PSD) functions of the two time series and $h_{xy}(\nu)$ is the cross-spectrum (see eq. (3.2)). The coherence is a measurement of the linear corelation between two light curves as a function of the Fourier frequency and takes values between $0 < \gamma^2_{xy} \leq 1$. A value of 1 it shows perfect coherence while zero indicates that x and y are uncorrelated processes.

In this Section, we have assumed continuous time series $x(t)$ and $y(t)$. This is indeed the case with most processes in nature. But, in practice, we do not observe any object continuously but at regular time intervals $\Delta t_{bin}$. `EP16` studied the relation between the intrinsic, continuous time series $\{x(t),\ y(t)\}$ and the discrete version $\{X(t_p),\ Y(t_p)\}$ resulted from observations at regular intervals $t_p = p\Delta t_{bin}$ with $p = 1, 2, \ldots, N$ ($N$ is the total number of observations). They showed that $\{x(t),\ y(t)\}$ and $\{X(t_p),\ Y(t_p)\}$ have the same mean value, but different CCFs and CS and thus, the measured phase or time lags from observed light curves are not necessarily equal to the intrinsic phase or time lags of the continuous process. In the following section, we describe how we estimated the time-lags of a discrete light curves, introducing the so-called "cross-periodogram".

## 3.2 Time-lags estimation

Let us consider two evenly sampled light curves $x(t_r)$ and $y(t_r)$ corresponding, for example to the flux of an AGN at two different energy bands (i.e. 2–4keV and 4–7keV). Let us assume that the bin size of the light curves is $\Delta t_{bin}$ , and that there are N points in each light curve. Thus, the duration of the light curves is N $\Delta t_{bin}$. The discrete Fourier transform (DFT) of the time series $x(t_r)$ is defined as follows

$$X(\nu_p) = \sqrt{\frac{\Delta t_{bin}}{N}} \sum_{r=1}^{N} x(t_r) e^{-i2\pi\nu_p r\Delta t_{bin}}. \tag{3.7}$$

$X(\nu_p)$ is calculated at $N/2$ discrete frequencies $\nu_p = p/(N\Delta t_{bin})$, with $p = 1, 2, 3 \ldots N/2$. The highest frequency is the so-called Nyquist frequency, $\nu_{Nyq} = 1/(2\Delta t_{bin})$. An identical relationship holds for $y(t_r)$ and $Y(\nu_p)$:

$$Y(\nu_p) = \sqrt{\frac{\Delta t_{bin}}{N}} \sum_{r=1}^{N} y(t_r) e^{-i2\pi\nu_p r\Delta t_{bin}}. \tag{3.8}$$

The above eq. (3.7) and eq. (3.8) may also be written as

$$X(\nu_p) = \sqrt{\frac{\Delta t_{bin}}{N}} \left[ \sum_{r=1}^{N} x(t_r) \cos(2\pi\nu_p r\Delta t_{bin}) - i \sum_{r=1}^{N} x(t_r) \sin(2\pi\nu_p r\Delta t_{bin}) \right], \tag{3.9a}$$

$$Y(\nu_p) = \sqrt{\frac{\Delta t_{bin}}{N}} \left[ \sum_{r=1}^{N} y(t_r) \cos(2\pi\nu_p r\Delta t_{bin}) - i \sum_{r=1}^{N} y(t_r) \sin(2\pi\nu_p r\Delta t_{bin}) \right]. \tag{3.9b}$$

We define the cross-periodogram $I_{xy}(\nu_p)$ of the two light curves $x(t_r)$, $y(t_r)$, as follows,

$$I_{xy}(\nu_p) = X(\nu_p)Y^*(\nu_p), \tag{3.10}$$

where, the asterisk denotes the complex conjugate. The cross-periodogram (CP) can also be written in the complex form $I_{xy}(\nu_p) = \Re[I_{xy}(\nu_p)] - i\Im[I_{xy}(\nu_p)]$. We may calculate the real and imaginary parts

of the CP, by substituting eq. (3.9a) and eq. (3.9b) in eq. (3.10). Then, $\Re[I_{xy}(\nu_p)]$ and $\Im[I_{xy}(\nu_p)]$ are given by

$$\begin{aligned}\Re[I_{xy}(\nu_p)] = &\frac{\Delta t_{bin}}{N}\sum_{(r)}[x(t_r)\cos(2\pi\nu_p r\Delta t_{bin})]\sum_{(r)}[y(t_r)\cos(2\pi\nu_p r\Delta t_{bin})]+\\ &+\frac{\Delta t_{bin}}{N}\sum_{(r)}[x(t_r)\sin(2\pi\nu_p r\Delta t_{bin})]\sum_{(r)}[y(t_r)\sin(2\pi\nu_p r\Delta t_{bin})],\end{aligned} \tag{3.11a}$$

and,

$$\begin{aligned}\Im[I_{xy}(\nu_p)] = &\frac{\Delta t_{bin}}{N}\sum_{(r)}[x(t_r)\sin(2\pi\nu_p r\Delta t_{bin})]\sum_{(r)}[y(t_r)\cos(2\pi\nu_p r\Delta t_{bin})]+\\ &+\frac{\Delta t_{bin}}{N}\sum_{(r)}[x(t_r)\cos(2\pi\nu_p r\Delta t_{bin})]\sum_{(r)}[y(t_r)\sin(2\pi\nu_p r\Delta t_{bin})].\end{aligned} \tag{3.11b}$$

The cross-periodogram is used in practice as an estimator of the CS. `EP16` performed an extensive number of simulations to quantify the statistical properties of the cross-periodogram. They found that in the case of sampled light curves, time-lags should be estimated up to a maximum frequency $\nu \leq \nu_{Nyq}/3$. At higher frequencies the cross-periodogram is a biased estimator of the cross-spectrum. They also suggested that one should chop a light curve into smaller segments, estimate the cross-periodogram of each one, and accept the mean of the individual cross-periodograms at each frequency as the estimator of the cross-spectrum at that frequency.

Therefore, we break the light curve into $n_s$ segments of length $T_s$ with $N_s^{obs}$ points for each segment ($T_s = N_s^{obs}\Delta t_{bin}$), and we average the $n_s$ individual cross-periodograms at each frequency to compute the average cross-periodogram $\hat{h}_{xy}$ as follows

$$\hat{h}_{xy}(\nu_p) = \frac{1}{n_s}\sum_{k=1}^{n_s} I_{xy}^{(k)}(\nu_p). \tag{3.12}$$

Just like the CS, the average cross-periodogram is also a complex number, hence $\hat{h}_{xy}(\nu_p) = \Re[\hat{h}_{xy}(\nu)] - i\Im[\hat{h}_{xy}(\nu)] = [\hat{h}_{xy}(\nu_p)]e^{-i\hat{\phi}_{xy}(\nu)}$, where $|\hat{h}_{xy}(\nu_p)| = \sqrt{\Re[\hat{h}_{xy}(\nu)]^2 + \Im[\hat{h}_{xy}(\nu)]^2}$ and,

$$\hat{\phi}_{xy}(\nu_p) = \arctan\left[-\frac{\Im[\hat{h}_{xy}(\nu_p)]}{\Re[\hat{h}_{xy}(\nu_p)]}\right] = \arg[\hat{h}_{xy}(\nu_p)], \tag{3.13}$$

is the estimator of the intrinsic phase-lag. Then, the estimate of the time-lag at each frequency is simply given by

$$\hat{\tau}_{xy}(\nu_p) = \frac{\arg[\hat{h}_{xy}(\nu_p)]}{2\pi\nu_p}. \tag{3.14}$$

According to `EP16`, when $n_s \geq 20$, the time-lag estimates defined by eq. (3.14) above are Gaussian variables and their error is given by

$$\hat{\sigma}_{\hat{\tau}}(\nu_p) = \frac{1}{2\pi\nu_p}\frac{1}{\sqrt{2n_s}}\sqrt{\frac{1-\hat{\gamma}_{xy}^2(\nu_p)}{\hat{\gamma}_{xy}^2(\nu_p)}}, \text{where,} \tag{3.15}$$

$$\hat{\gamma}_{xy}^2(\nu_p) = \frac{|\hat{h}_{xy}(\nu_p)|^2}{\hat{h}_x(\nu_p)\hat{h}_y(\nu_p)}, \tag{3.16}$$

$\hat{\gamma}_{xy}(\nu_p)$ is the estimator of the coherence function and $\hat{h}_x(\nu_p)$ and $\hat{h}_y(\nu_p)$ are the periodograms[1] of the light curves. The coherence estimate is a biased estimator of the intrinsic coherence of the measured process, due to the Poisson noise in the light curves. Even if the intrinsic coherence is equal to unity, the coherence estimate is decreasing exponentially as the Fourier frequency increases and converges to $1/n_s$. `EP16` showed that the coherence estimate is well fitted by the following equation:

$$\hat{\gamma}^2_{xy}(\nu) = \left(1 - \frac{1}{n_s}\right) \exp\left[-(\nu/\nu_0)^q\right] + \frac{1}{n_s}. \tag{3.17}$$

According to `EP16`, the time-lag estimates are unbiased up to a maximum frequency $\nu_{crit}$ where $\nu_{crit}$ is the smallest value of either $\nu_{Nyq}/3$ (as we mentioned above) or the frequency at which $\hat{\gamma}^2_{xy}(\nu_{crit}) = 1.2/(1+0.2n_s)$. In the following sections we present the results for the time-lag and coherence estimates of the three sources we discussed in the Chapter 2.

## 3.3 Time-lags of MCG-6–30–15

In Chapter 2, we examined the light curves of MCG-6–30–15. We created 3 groups of light curves with similar cadence of observations, listed in Table 2.2. For all light curves in each group we linearly interpolate to produce equidistance light curves with a $\Delta t_{bin}$ that produces points with the least time difference from the observations of the group. This process is discussed in detail in Section 2.1. We can now use the resulting segments to estimate the time-lags between the 2–4 and 4–7 keV, as well as the time-lags between 2–4 and 7–10 keV bands (i.e. the "S-vs-H1" and the "S-vs-H2" respectively).

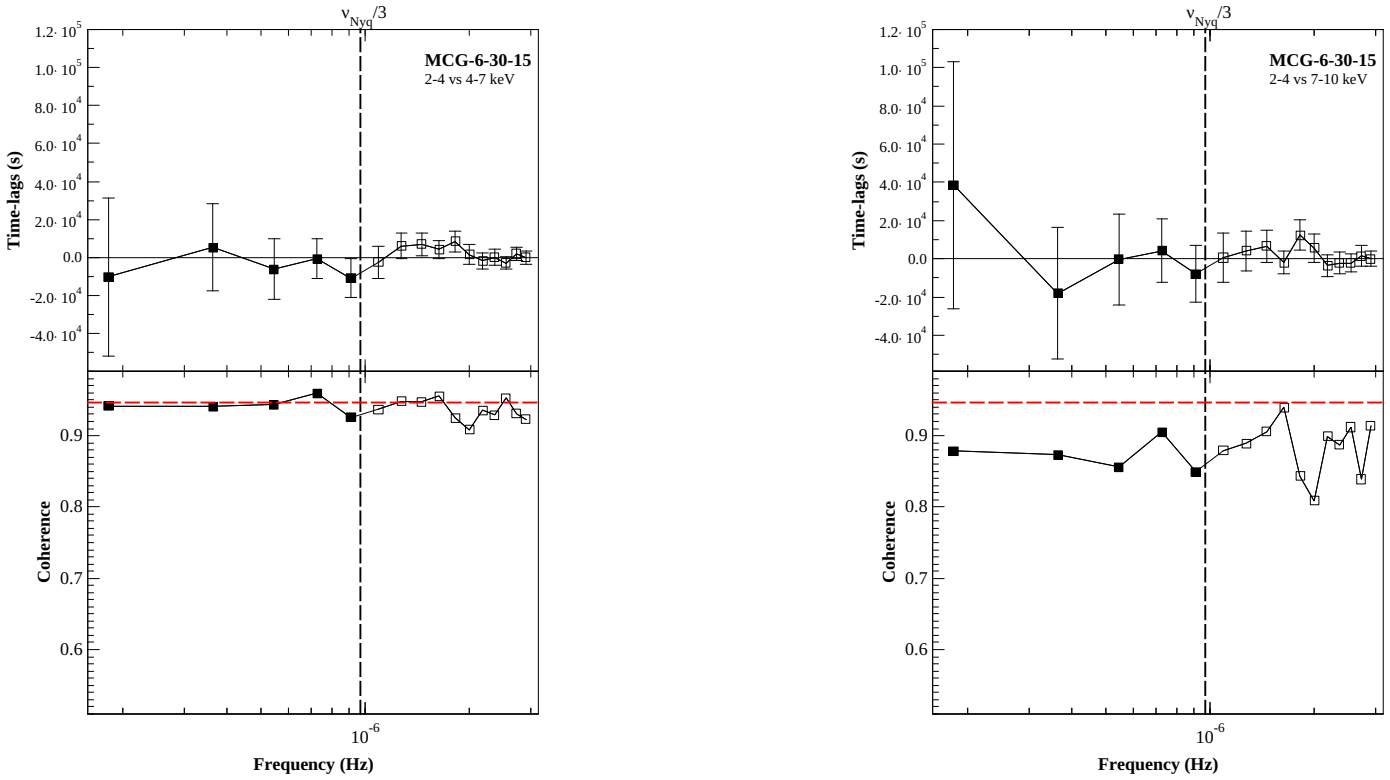


**Figure 3.1:** The "S-vs-H1" and "S-vs-H2" (left and right panel respectively) time-lags and coherence estimates for "Group A" light curve segments of MCG-6–30–15.

[1]The periodograms are estimators of the PSD and are defined as the square modulus of the DFT of the light curve (i.e. $|X(t_p)|^2$.

We divide the light curves in Group A into $n_s = 19$ smaller segments with duration $T_s = 62d$. We used eqs. (3.10), (3.11a) and (3.11b) to compute the cross-spectrum of each segment. Then, we average the cross-periodograms of all segments to estimate the CS, and using eq. (3.14) and eq. (3.16) we estimate the time-lags and coherence at frequencies $2.9 \times 10^{-6} Hz \leq \nu \leq 1.9 \times 10^{-7} Hz$. The results are plotted at Fig. (3.1). The top left and right panel shows the "S-vs-H1" and "S-vs-H2" time-lags respectively, and the bottom panel shows the sample coherence. Since the sample coherence is very large, we consider the sampled time-lags to be reliable estimates of the intrinsic time-lags up to $\nu = \nu_{Nyq}/3$. This frequency is indicated by the vertical line on the plots. The red dashed line in the coherence plots indicate the value $(1 - 1/n_s)$. According to eq. (3.17), this is the value of the sampled coherence at low frequencies ($\nu \ll \nu_0$) if the intrinsic coherence is one.

Just like above we computed the cross-periodogram, the averaged cross-periodogram, the time-lags and the coherence for the light curves of Group B. We used a bin size of $\Delta t_{bin} = 3.98d$ and we divided the light curves into 15 segments with duration $119.4d$. The use of Group B light curves allowed us to estimate time-lags at even lower frequencies, from $9.7 \times 10^{-8} Hz$ up to $1.5 \times 10^{-6} Hz$. The results are plotted in Fig. (3.2).

Group C consists of the longest light curve parts. We divided them into 19 segments with duration $T_s = 243.2d$ to estimate time-lags at lower frequencies than the previous groups of light curves. Adopting $\Delta t_{bin} = 12.8d$, we estimated the time-lags at frequencies $4.8 \times 10^{-8} Hz \leq \nu \leq 4.5 \times 10^{-7} Hz$, as shown in Fig. (3.3).

All time-lags in Fig. (3.1), (3.2) and (3.3) are consistent with zero (within one sigma). Additionally, the "S-vs-H1" sampled coherence matches the dashed horizontal line, indicating that the intrinsic coherence between the 2-4 and 4-7 keV bands is equal to unity. However, this is not true for the "S-vs-H2" case. The sampled coherence is systematically lower than the value we would expect if the intrinsic coherence is one.

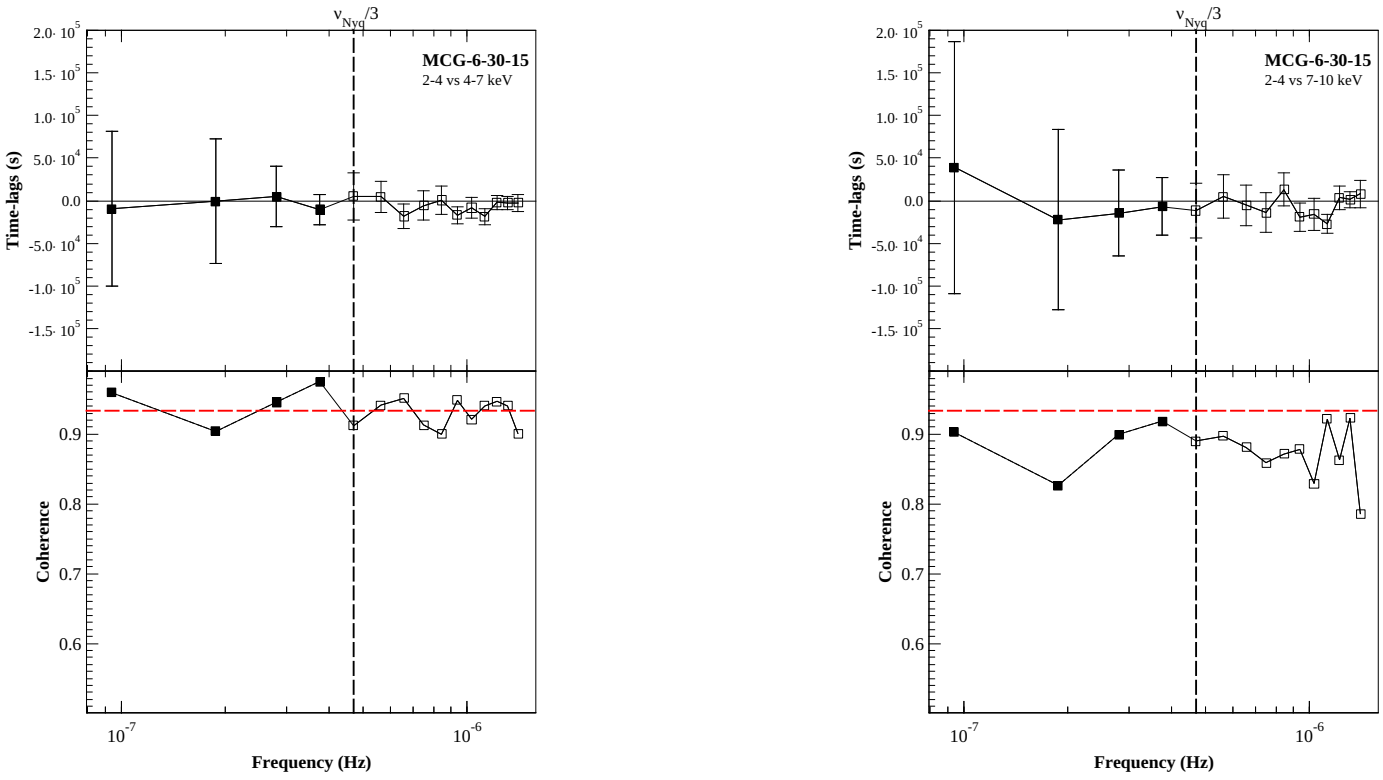


**Figure 3.2:** The "S-vs-H1" and "S-vs-H2" (left and right panel respectively) time-lags and coherence estimates for "Group B" light curve segments of MCG-6–30–15.

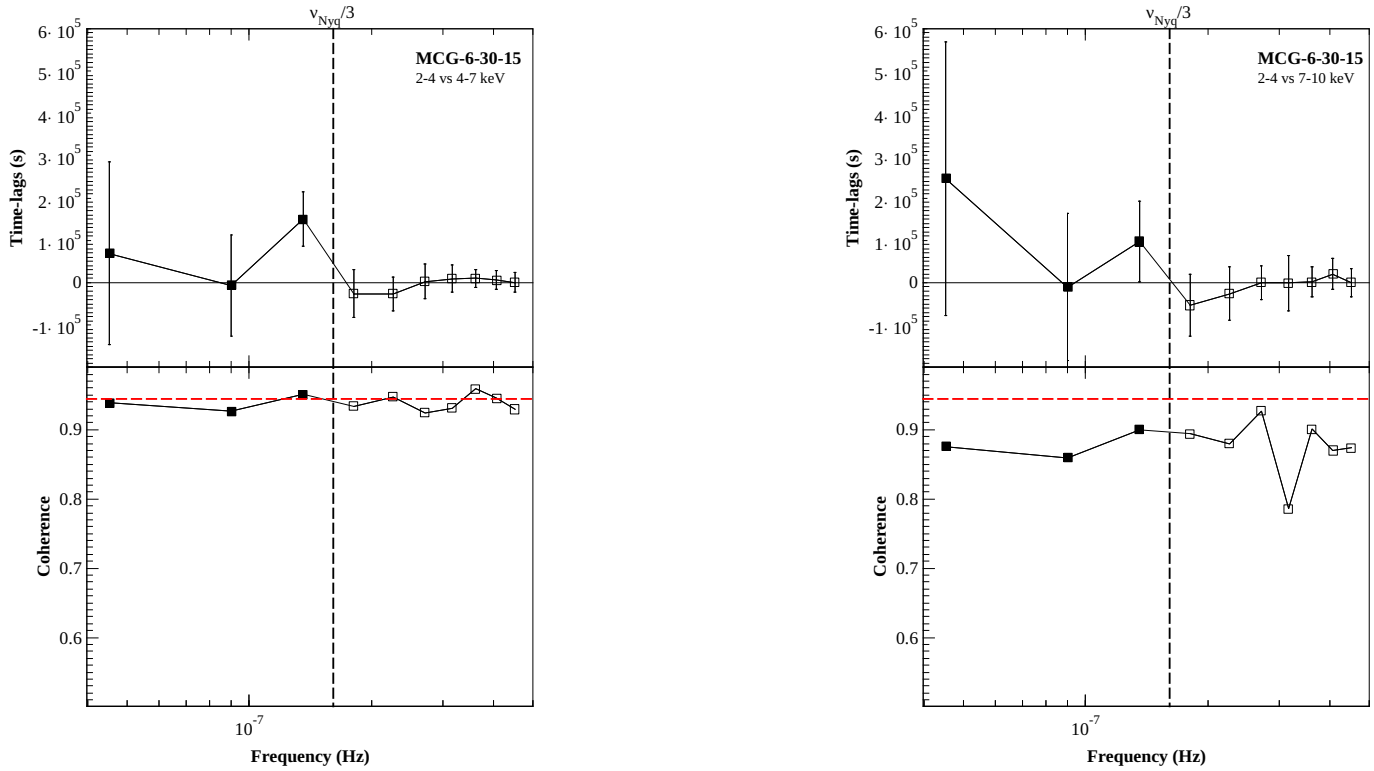


**Figure 3.3:** The "S-vs-H1" and "S-vs-H2" (left and right panel respectively) time-lags and coherence estimates for "Group C" light curve segments of MCG-6–30–15.

We end up with 12 reliable time-lag estimates of MCG-6–30–15 when we use all segments in Groups A, B and C. We plot them all in Fig. (3.4) (open, red circles). The time-lags cover a rather large frequency range from $\sim 5 \times 10^{-8} Hz$ up to $\sim 10^{-6} Hz$. In order to reduce their error, we binned them over groups of 4 frequencies. The black squares in Fig. (3.4) shows the resulting (weighted) average time-lags. The vertical bars show the error of the mean, while the horizontal bar indicates the frequency range over which we averages the original time-lags. We consider the binned time-lags as our final estimate of the low frequency time-lags in MCG-6–30–15.

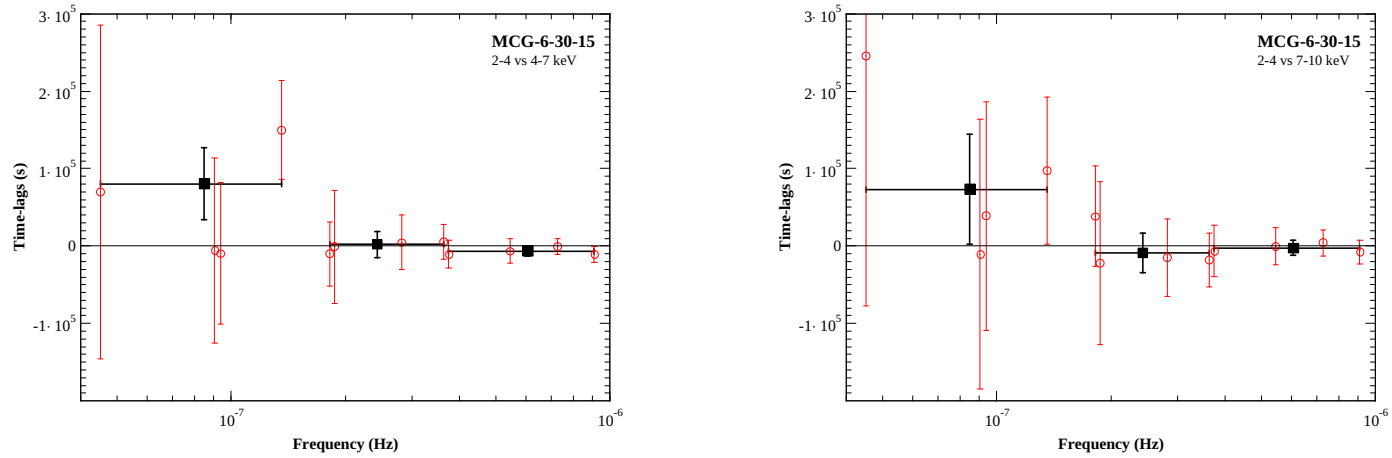


**Figure 3.4:** The "S-vs-H1" and "S-vs-H2" (left and right panel respectively) time-lags of MCG-6–30–15. The black filled squares show the mean time-lags and the horizontal error bars show the bin's width.

## 3.4 Time-lags of Ark 564

We considered the two groups of segments listed in Table 2.4 under the label "Group A" and "Group B" respectively. The first group contains all available light-curve segments, and the second group contain segments with a high cadency of observation. They can be used to estimate time-lags at high frequencies. Following the same method as we did for MCG-6–30–15, for the first group we used $\Delta t_{bin} = 4.27d$ and divide the light curve into 21 segments with duration $T_s = 68.32d$. We computed the cross-periodogram of each segment, the average cross-periodogram, the time-lags and the coherence from $1.7 \times 10^{-7} Hz$ up to $1.4 \times 10^{-6} Hz$. The light curves of the second group were divided into 17 short segments with duration $T_s = 1.703d$ and $\Delta t_{bin} = 0.131d$. Therefore, using the Group B segments, we can estimate the time-lags and coherence at higher frequencies than Group A, from $\nu \geq 6.8 \times 10^{-6} Hz$ up to $4.4 \times 10^{-5} Hz$.

The results are plotted in Figs. (3.5) and (3.6) for the Groups A and B respectively. The dashed vertical line indicates $\nu_{Nyq}/3$.Time-lags estimates at frequencies lower than $\nu_{Nyq}/3$ are reliable estimates of the intrinsic time-lags when the sampled coherence is higher than a critical value of $1.2/(1 + 0.2n_s)$ (see Section 3.2). In our case, $1.2/(1 + 0.2n_s) = 0.23$ for "S-vs-H1" and 0.27 for "S-vs-H2". The "S-vs-H1" sample coherence is higher than the critical value both for group A and B, thus, the time-lags at frequencies lower than $\nu_{Nyq}/3$ should be unbiased. However, the 2–4 vs 7–10 keV sample coherence of the second frequency point in Group A is lower than the critical value (see bottom plot, in right panel if Fig. (3.5)). In this case, the true scatter of time-lags around the mean may not be a Gaussian and eq. (3.15) may underestimates the time-lag error.

Similarly with MCG-6–30–15, the time-lags are consistent with zero for both groups and the "S-vs-H2" sample coherence is lower than "S-vs-H1". The dashed horizontal indicates the value we would expect for the sample coherence if the intrinsic coherence is one. For both "S-vs-H1" and "S-vs-H2" cases, the sample coherence is lower than the dashed horizontal line indicating that the instinct

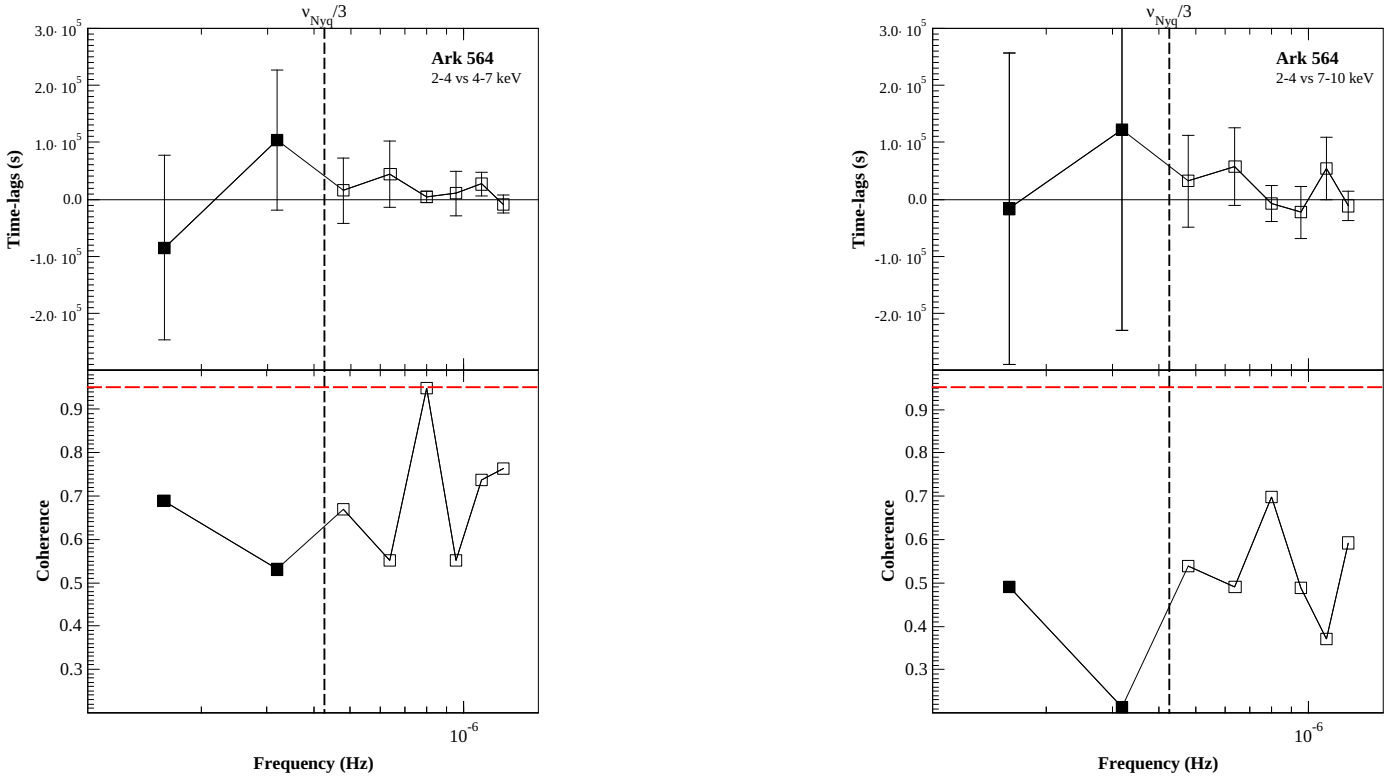


**Figure 3.5:** The "S-vs-H1" and "S-vs-H2" (left and right panel respectively) time-lags and coherence estimates for "Group A" light curve segments of Ark 564.

coherence is lower than one contrary to MCG-6–30–15 where the intrinsic coherence is one for the "S-vs-H1" time-lags.

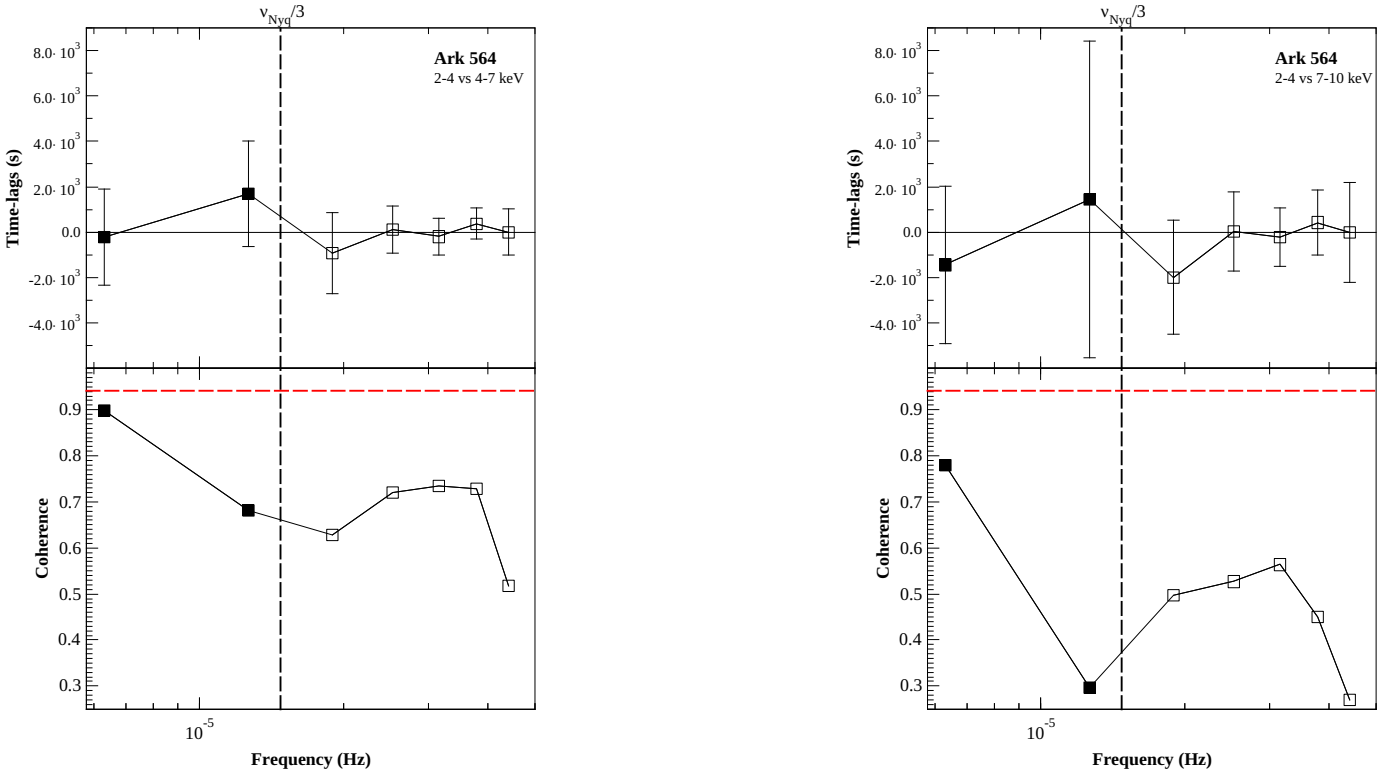


**Figure 3.6:** The "S-vs-H1" and "S-vs-H2" (left and right panel respectively) time-lags and coherence estimates for "Group B" light curve segments of Ark 564.

Fig. (3.7) shows the "S-vs-H1" and the "S-vs-H2" time-lags (left and right panel, respectively) at frequencies lower than $\nu_{Nyq}/3$, using the Group A and Group B light curves. The figure shows clearly the difference in the time-lags of the two Groups. To reduce the error of the time-lags, we binned the Group A and Group B time-lags together and calculate their (weighted) average time-lag. The black squares show the average time-lag and their error, while the horizontal error bar indicates the bin width.

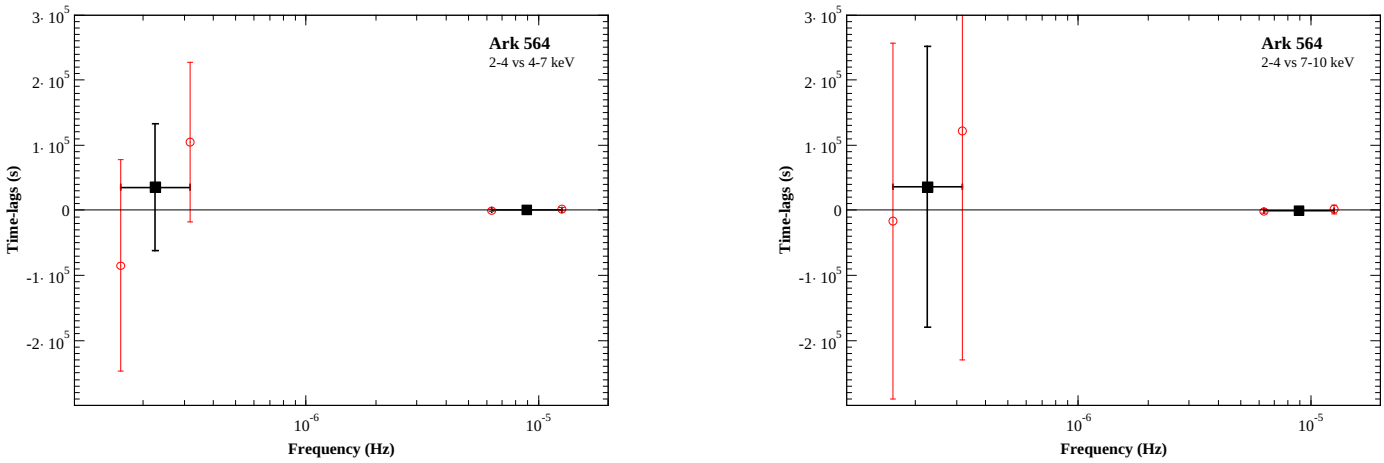


**Figure 3.7:** The "S-vs-H1" and "S-vs-H2" (left and right panel respectively) time-lags of Ark 564. The black filled squares show the mean time-lags and the horizontal error bars show the bin's width.

## 3.5 Time-lags of Mkn 766

We used all available light curves of Mkn 766 to estimate time-lags at a wide range of frequencies. First, we divided them into 22 segments with duration $T_s = 111d$. Using eqs. (3.10) and (3.11a), (3.11b) we computed the cross-periodogram of each segment and then, we average the cross-periodograms of all segments to estimate the cross-spectrum. By the use of eq. (3.14) and eq. (3.16) we estimate the time-lags and coherence at frequencies $10^{-6}Hz \leq \nu \leq 10^{-7}Hz$.

Fig. (3.8) shows the results. The 2–4 vs 4–7 keV and 2–4 vs 7–10 keV time-lags and coherence are given in the left and right panel of Fig. (3.8) respectively. For both cases the sample coherence is higher than the critical value at all frequencies, therefore, the dashed vertical line at $\nu = \nu_{Nyq}/3$ indicates the frequency up to which we can reliably measure time-lags. The dashed horizontal line in the same plot, shows the value $1 - 1/n_s$ which is the value we would expect for the sampled coherence at low frequencies, if the intrinsic coherence is one.

In the previous sources, the "S-vs-H1" sample coherence is higher than the "S-vs-H2". This is also true for Mkn 766 however, in this source the "S-vs-H1" and "S-vs-H2" coherence estimates differ only slightly. Additionally, the sample coherence in both "S-vs-H1" and "S-vs-H2" plots is lower than the dashed horizontal line hence, the intrinsic coherence is probably lower than one in both cases.

All the reliable estimates of the time-lags are plotted in Fig. (3.9) with red, open circles. To reduce their errors, we binned them over groups of two (black filled squares) and all together (open squares). The black filled and open squares show the resulting (weighted) mean. The vertical error bars indicate the error of the mean and the horizontal bar indicates the bin width. The time-lags of Mkn 766 are negative which imply that the variations in the hard band appear first with respect to the variations of the 2–4 keV band (the soft band is delayed with respect to the hard band). The mean 2–4 vs 4–7 keV time-lag is $-75000 \pm 34000s$ and $-71000 \pm 35000s$ for the 2–4 vs 7–10 keV case.

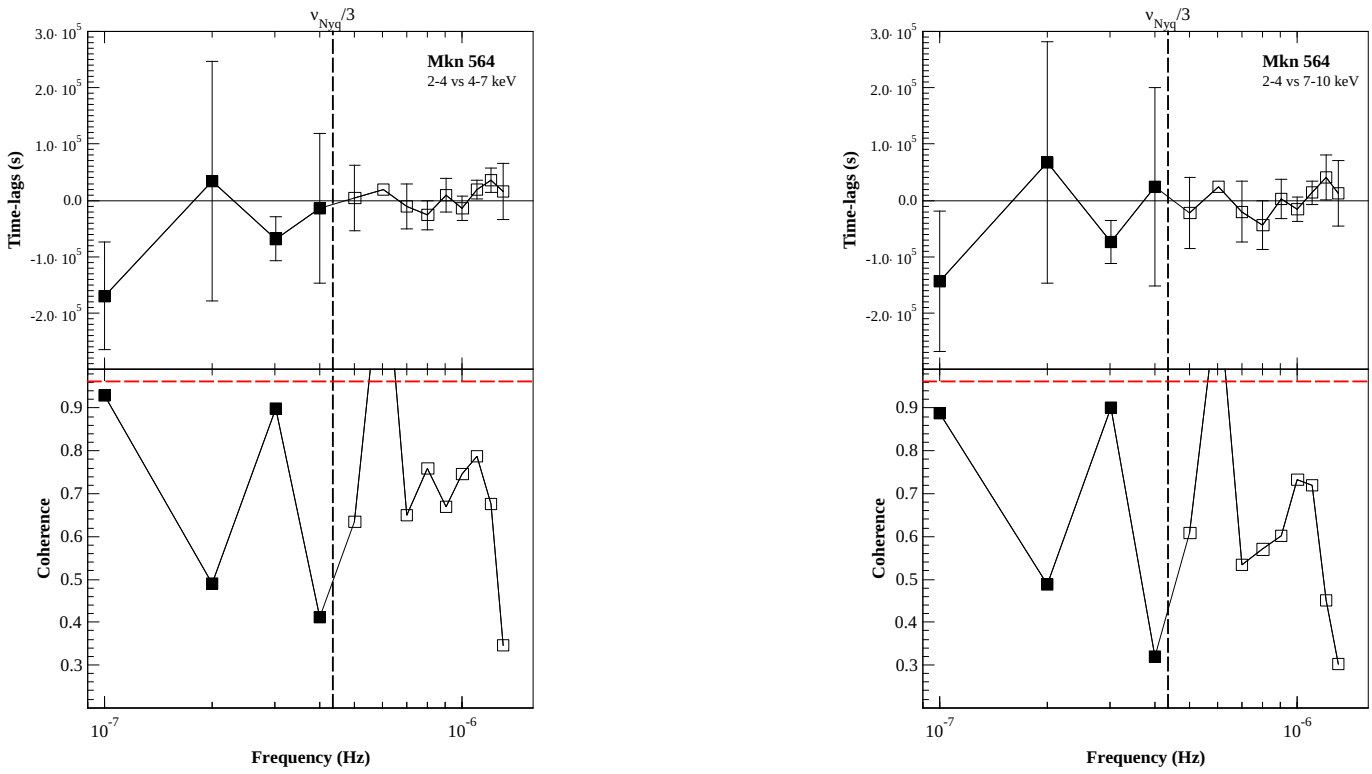


**Figure 3.8:** The "S-vs-H1" and "S-vs-H2" (left and right panel respectively) time-lags and coherence estimates of Mkn 766 light curve segments.

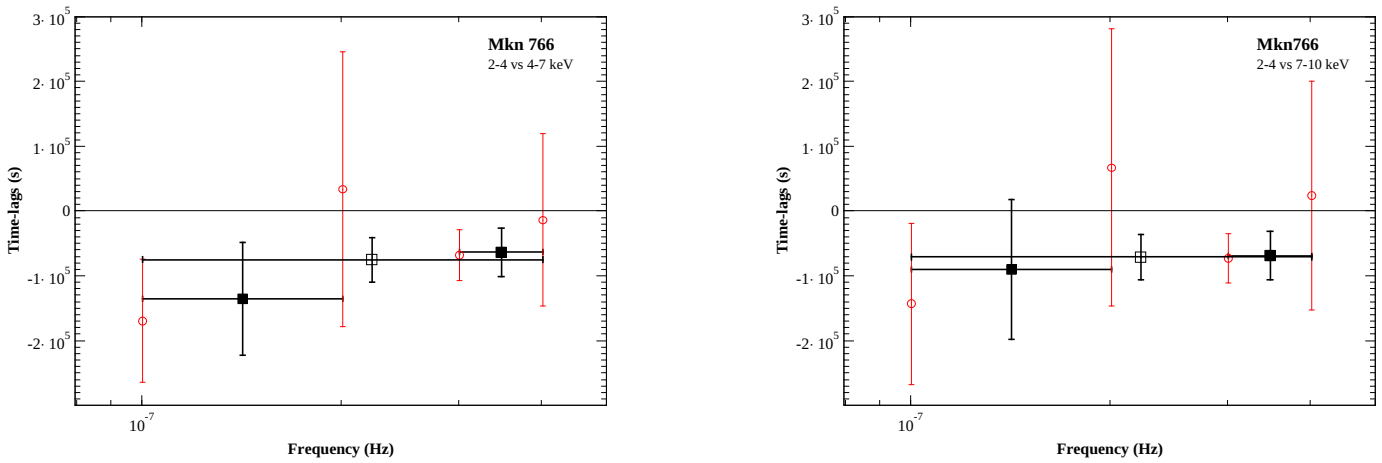


**Figure 3.9:** The "S-vs-H1" and "S-vs-H2" (left and right panel respectively) time-lags of Mkn 766. The black filled and open squares show the mean time-lags and the horizontal error bars show the bin's width.

## 3.6 Bias of the time-lag estimates due to finite light curve duration

In the previous section, we estimated the time-lag of MCG-6–30–15, Ark 564 and Mkn 766. As suggested by EP16 (for sampled light curves), we considered reliable estimates of time-lags at frequencies $< \nu_{Nyq}/3$. At higher frequencies time-lag bias noticeable increases due to aliasing effect. However, time-lags are biased even at low frequencies due to the finite light curve segments duration.

To quantify the time-lag bias in terms of the intrinsic value EP16 introduced the following quantity:

$$\delta_\tau(\nu_p) = \frac{\tau_{int}(\nu_p) - \langle \hat{\tau}_{obs}(\nu_p) \rangle}{\tau_{int}(\nu_p)}, \tag{3.18}$$

where $\tau_{int}$ is the model intrinsic time-lag and $\langle \hat{\tau}_{obs}(\nu_p) \rangle$ is the measured time-lags[2], so $\delta_\tau(\nu_p)$ shows the relative difference between the model and the observed time-lags. EP16 conducted a series of numerical experiments to find the dependence of light curve duration ($T_s$) on time-lag bias. They found that the mean time-lag bias decreases with increasing $T_s$ as $1/\sqrt{T_s}$.

Then, for the same value of $T_s$, EP16 measured $\delta_\tau$ at different frequencies. Fig. (4) of EP17 show the time-lag bias as a function of frequency for light curves with different duration from 3.2ks to 512ks $\approx$ 6d. At low frequencies, time-lag bias has roughly the same slope. We measured from Fig. (4) of EP17, $\delta_\tau(\nu) \propto \nu^{-0.7}$.

Based on the results of EP17, we can assume that the proportionality constant at a frequency $\nu$ will follow the same relation with the mean time-lag bias ($\propto 1/\sqrt{T}$). As follows, the relation of the time-lag bias and frequency is

$$\delta_\tau(\nu) = \sqrt{\frac{T_{\rm exp}}{T_s}} A_{\rm exp} \left(\frac{\nu}{\nu_0}\right)^{-0.7} \tag{3.19}$$

where, $T_{\rm exp}$ is the light curve duration of EP16 experiment and $A_{\rm exp}$ is the amplitude of the time-lag bias at frequency $\nu_0$. At $\nu_0 = 10^{-5} Hz$ the amplitude of the relative time-lag bias for the light curves with $T_{\rm exp} = 512ks$ is $A_{\rm exp} = 0.08$.

[2]In EP16 $\langle \hat{\tau}_{obs}(\nu_p) \rangle$ is the sample mean at each frequency.

# Chapter 4: Comparison with the high frequency time-lags

The low frequency time-lags estimates of MCG-6–30–15, Ark 564 and Mkn 766 can provide more information regarding the physical processes in these sources, if we can combine them with time-lag estimates at higher frequencies. `EP17` used `XMM-Newton` data of 10 bright AGN sources (including MCG-6–30–15, Ark 564 and Mkn 766), and they measured time-lags at frequencies from $5 \times 10^{-5} Hz$ to $\sim 10^{-3} Hz$ between various energy bands in the range 0.5–10 keV, and the 2–4 keV band, which they choose as the reference band. In this chapter we will investigate if the time-lags at low ($RXTE$) frequencies we estimated in Chapter 3 are consistent with the time-lag estimates at higher frequencies.

## 4.1 Extrapolation of the time-lag model at low frequencies

`EP17` found that the time-lags between one energy band with mean energy $\overline{E}$ and the 2–4 keV band (with a mean energy of 3keV) can be well approximated by a power law function of the form:

$$\hat{\tau}(\nu,\ \overline{E}) = A_0 \log(\overline{E}/3keV)(\nu/10^{-4}Hz)^{-s}, \tag{4.1}$$

where $A_0$ corresponds to the time-lag at $\nu = 10^{-4} Hz$. The equation above shows that the time-lags have a power law dependence on frequency, with a slope which is $\sim -1$ in all sources. The time-lags amplitude increases with increasing difference between the energy of the bands. In this work we used light curves in the 4–7 and 7–10 keV bands with mean energy $\overline{E} = 5.5$keV and 8.5keV, respectively, and as the reference band we also used 2–4 keV (with $\overline{E} = 3$keV). `EP17` measured the slope, s, and the amplitude, $A_0$, using XMM-Newton data and they found that $s = 1.3 \pm 0.3$, $A_0 = 321 \pm 26s$ for MCG-6–30–15, $s = 1.4 \pm 0.1$, $A_0 = 618 \pm 81s$ for Ark 564, and $s = -0.1 \pm 0.3$, $A_0 = 63 \pm 37s$ for Mkn 766. Using those values we can extrapolate eq. (4.1) at low frequencies and compare it with our results from Chapter 3.

### 4.1.1 MCG-6–30–15 & Ark 564

Figs. (4.1) and (4.2) present our results for MCG-6–30–15 and Ark 564. The black filled squares indicate the (binned) time-lags estimates we measured in Chapter 3. The vertical error bars show the time-lag error, while the horizontal error bars show the bin's width. The continuous solid lines show the extrapolation of eq. (4.1) at frequencies lower than $10^4 Hz$. The dashed lines show the $1\sigma$ uncertainty of the `EP17` time-lag model. We used eq. (4.1) to compute these lines with $A_0 \pm 1\sigma_{A_0}$ and $s \pm 1\sigma_s$, as needed in order to identify the $1\sigma$ confidence area around the best fit line. The black arrow at the highest frequency in the left panel of Fig. (4.1), indicates the $3\sigma$ upper limit of the respective time-lags estimate, which is negative in this case.

In general, the low-frequency time-lags estimates are consistent with the extrapolation of the high frequency best-fit model to lower frequencies. However all time-lags, both in MCG-6–30–15 and Ark 564

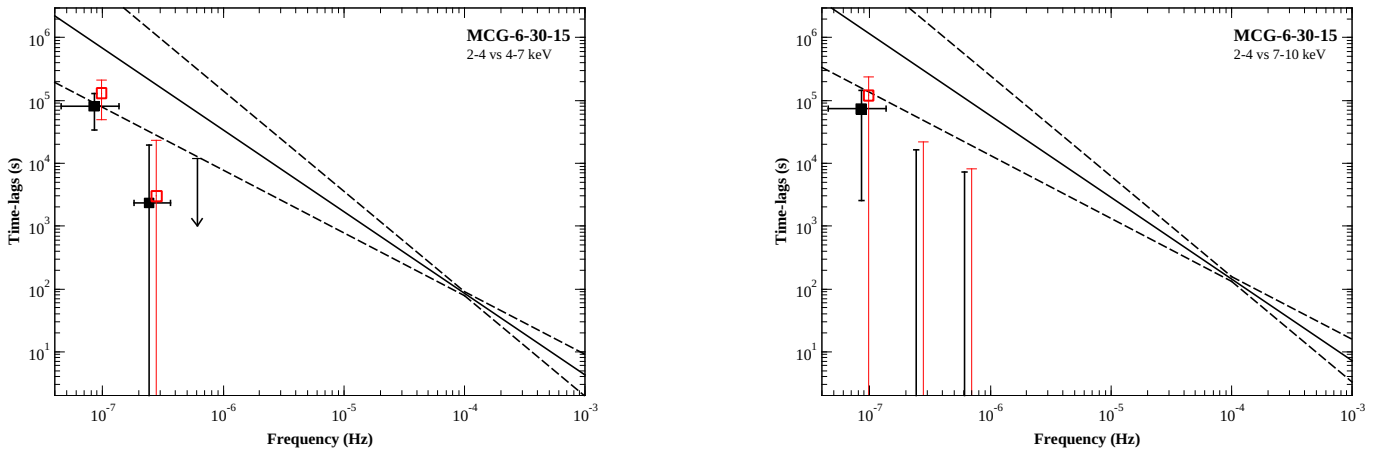


**Figure 4.1:** The extrapolation of XMM-Newton time-lag fit (EP17) to low (*RXTE*) frequencies for MCG-6–30–15.

are below the extrapolated high frequency model. This could be the result of the low frequency bias in the time-lag estimates. As we have discussed in Chapter 3, the main factors that contribute to the bias of the time-lag estimates is the fact that light curves are observed at regular time intervals, and the finite light curve duration. As EP16 suggested, to avoid the bias due to the former factor, we consider time-lags only at frequencies $\leq \nu_{Nyq}/3$. The finite duration of the light curves also contribute to bias at low frequencies, as we discussed in Section 3.6. According to eq. (3.19) the bias due to the finite light curve duration depends on the frequency. In principle, we can use eq. (3.19) to calculate the relative time-lag bias at each frequency and then "correct" the estimated time-lags. We discuss the calculation of the relative bias, and the subsequent correction at the observed time-lags in the next paragraphs.

### The relative bias of MCG-6–30–15

In Chapter 3 we estimated MCG-6–30–15 time-lags at 12 frequencies and then we binned them into groups of 4 frequencies. The resulting frequency of the MCG-6–30–15 time-lags (i.e. the average of the logarithms of all the frequencies inside each bin) is $\nu = 8.5\times10^{-8}$, $2.4\times10^{-7}$ and $6\times10^{-7}Hz$. The time-lag estimate at the lowest frequency (at $\nu = 8.5\times10^{-8}$), is the average of 3 time-lags computed with Group C light curves with duration 240d and one time-lag from Group B light curves with $T_s = 120d$. For an approximate estimate of the relative time-lag bias we accept $T_s = 200d$. Using eq. (3.19), we measure a relative time-lag bias of $\delta_\tau(\nu = 8.5\times10^{-8}Hz) = 0.4$. For the other two frequencies, we used light curves with $T_s = 60d$ and $120d$, or on average $T_s = 90d$ and the relative time-lag bias in the case is $\delta_\tau(\nu = 2.4\times10^{-7}Hz) = 0.27$ and $\delta_\tau(\nu = 6\times10^{-7}Hz) = 0.14$.

To calculate the unbiased time-lags, we solve eq. (3.18) for the intrinsic time-lags, and we get:

$$\tau_{int}(\nu_p) = \frac{\hat{\tau}_{obs}(\nu_p)}{1-\delta\tau(\nu_p)} \tag{4.2}$$

Substituting the values we calculated above for $\delta\tau(\nu_p)$, and the observed time-lags at each frequency, we can use eq. (4.2) to compute the unbiased, time-lag estimates. Red open squares in Fig. (4.1) indicate these estimates. For clarity reasons, the unbiased time-lags are slightly shifted to the right. The new estimates are 1.1–1.2 times larger than the previous estimates. As a result, they are closer to the extrapolated high frequency time-lags, although they are still lower than the extrapolation of the high frequency model time-lags.

Equation 4.2 cannot work if the time-lag estimates are negative. For the negative time-lag values we measured the deviation of the time-lag estimates from the extrapolation of the EP17 model at

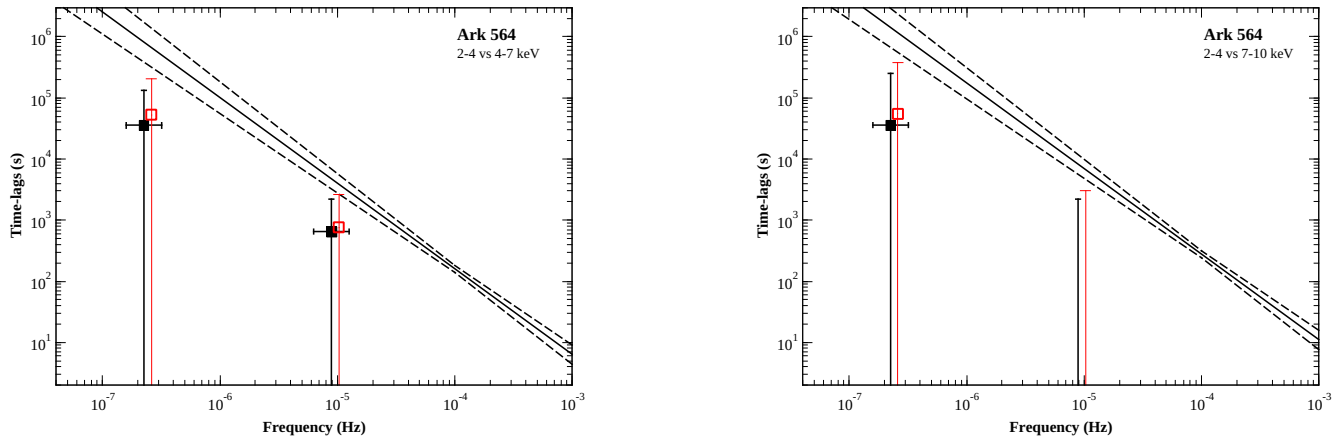


**Figure 4.2:** The extrapolation of XMM-Newton time-lag fit (`EP17`) to low (*RXTE*) frequencies for Ark 564.

low frequencies. In the case of the 2–4 vs 4–7 keV time-lags, we measured $\hat{\tau}_{obs} = -6500 \pm 6000s$ at $\nu = 6 \times 10^{-7}Hz$. The `EP17` model extrapolation at $6 \times 10^{-7}Hz$ gives $\tau_{EP17} = (6.5 \pm 5.3) \times 10^4 s$. Therefore, $\Delta\tau = \tau_{EP17}(6 \times 10^{-7}Hz) - \hat{\tau}_{obs}(6 \times 10^{-7}Hz) = (7.1 \pm 5.3) \times 10^4 s$. In the case of the 2–4 vs 7–10 keV time-lags, we measured two negative time-lags: $\hat{\tau}_{obs}(2.4 \times 10^{-7}Hz) = (-1 \pm 3) \times 10^4 s$ and $\hat{\tau}_{obs}(6 \times 10^{-7}Hz) = -2500 \pm 9500s$. The extrapolation of the `EP17` model at these frequencies give $\tau_{EP17}(2.4 \times 10^{-7}Hz) = (3.7 \pm 3.0) \times 10^5 s$ and $\tau_{EP17}(6 \times 10^{-7}Hz) = (1.0 \pm 0.8) \times 10^4 s$. Therefore $\Delta\tau(\nu = 2.4 \times 10^{-7}Hz) = (3.8 \pm 3.0) \times 10^5 s$ and $\Delta\tau(\nu = 6 \times 10^{-7}Hz) = (1.0 \pm 0.8) \times 10^5 s$. Due to the large uncertainty of the extrapolated high frequency model time-lags, all the differences between the observed time-lags and he extrapolation of the $\tau_{EP17}$ model are not significant (they are within 1.25–1.35$\sigma$).

### The relative bias of Ark 564

Similarly with MCG-6–30–15 we will calculate the relative bias of Ark 564 using eq. (4.2). As we described in Section 3.4 we ended up with 4 reliable estimates of time-lags for Ark 564, and we binned the into groups of two. For the first frequency ($\nu_1 = 2.25 \times 10^{-7}Hz$) we used light curves with $T_s = 68d$, thus $\delta_\tau(\nu_1) = 0.34$. For the second frequency bin we used light curves we used much sorter light curves ($T_s = 1.7d$) and the relative bias in this case is $\delta_\tau(\nu = 9 \times 10^{-6}Hz) = 0.16$. Then, solving eq. (3.18) for the intrinsic time-lags we found the unbiased time-lags due to finite light curve duration. Fig. (4.2) show the results.

For the negative time-lag estimate at $\nu = 9 \times 10^{-6}Hz$, in the case of 2–4 vs 7–10 keV time-lags, we measure the deviation of the time-lag estimate from the extrapolation at low frequencies. $\hat{\tau}_{obs}(9{\times}10^{-6}Hz) = -870{\pm}3100s$ and $\tau_{EP17}(9{\times}10^{-6}Hz) = (8.2{\pm}2.3){\times}10^3 s$ therefore, $\Delta\tau = (9{\pm}4){\times}10^3 s$. This result indicates that the difference between our measurements and the high frequency time-lags when extrapolated at low frequencies is significant at the 2.4$\sigma$.

Even if we consider the bias of the measured time-lags due to the finite duration of the *RXTE* light curves all the observed frequencies of the time-lags are still bellow the extrapolation of the `EP17` model at low frequencies both for MCG-6–30-15 and Ark 564. The results are consistent, within errors, with the extrapolation of `EP17` model to lower frequencies however, the uncertainty of the extrapolation is very high at low frequencies.

## 4.2 Mkn 766

The time-lag spectra of all AGN that were studied by EP17 are well fitted by a power law with a slope of $\sim -1$. The only exception was Mkn 766, in this case the time-lag spectrum of this source remains almost constant at all frequencies estimated by EP17 ($s = 0.1 \pm 0.3$). Our result reinforce the EP17 results. The low frequency time-lags of Mrk 766 are negative at all frequencies both in the 2–4 vs 4–7 keV and the 2–4 vs 7–10 keV time-lags. They are fully consistent with the extrapolation of the EP17 model time-lags to lower frequencies within $1\sigma$. The fact that all the time-lag estimates are negative, suggests that indeed, the true time-lags may also be negative.

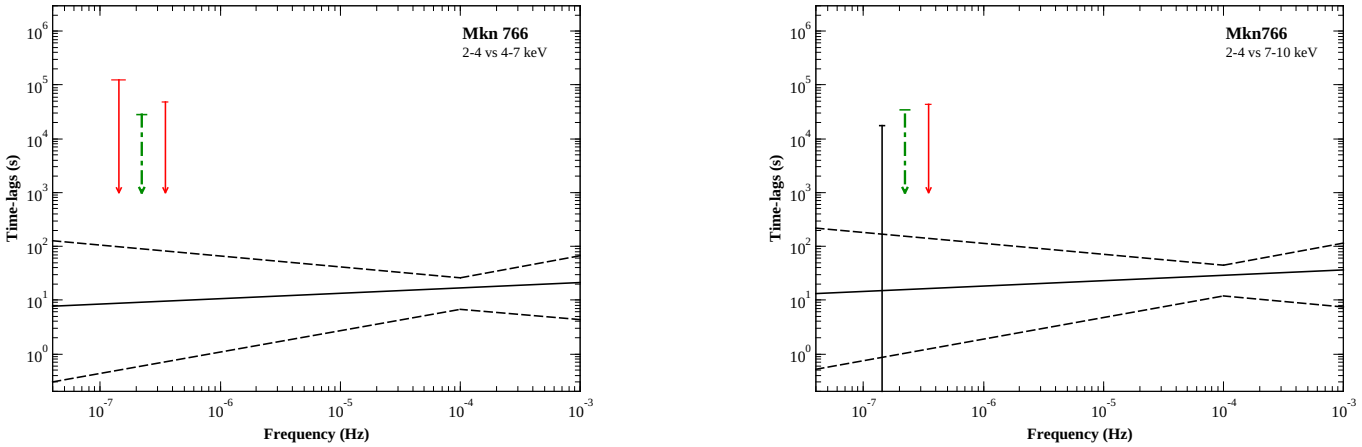


**Figure 4.3:** The extrapolation of XMM-Newton time-lag fit (EP17) to low (*RXTE*) frequencies for Mkn 766.

# Chapter 5: Summary & Conclusions

In this work, we studied the correlation between the observed variations in different energy bands of three AGN namely, MCG-6–30–15, Ark 564 and Mkn 766, using all available data from the *RXTE* database. We considered light curves in three energy bands (2–4, 4–7 and 7–10 keV) and we choose 2–4 keV as the reference band. We calculated the continuum time-lags following the `EP16` method and in this chapter we summarize our conclusions.

All three sources have been regularly observed by *RXTE* throughout its 16 years of operations. The cadence of observations varies, and minor as well as some major (i.e. 1–2 year long) gaps appear in the light curves. For a reliable estimation of the time-lags, we need evenly sampled light curves. For that reason, we divide the light curves into parts that include light curve segments with similar cadence of observations. We created three groups of segments in MCG-6–30–15 light curve, two groups for Ark 564 and we used all the available data of Mkn 766 in one group.

The first group in MCG-6–30–15 light curve includes 19 segments with a time difference between the observations of about 2 days ($\Delta t_{j-i,\ median} \sim 2d$). The length of each segment in this group is $\sim 62d$. For the light curve parts of the second group of segments, the source was observed about once every 4 days, allowing us to create 15 segments with each segment being $\sim 120d$ long. Finally, for the third group, we tried to identify the longest light curve parts that do not contain very large gaps.

To produce equidistant light curves from the various parts in each group, we followed a novel technique. For each group of light curve parts we considered various $\Delta t_{bin}$ values. For each $\Delta t_{bin}$, we linearly interpolate to produce equidistant light curves, and we measured the median time difference between the interpolated data points and the observation ($\Delta t_{dif,\ median}$). We choose the bin size that produces data points closer to the observations. For the first group we tested values from 1.1 to 2.3 days and found that $\Delta t_{bin} = 1.99d$ minimizes $\Delta t_{dif,\ median}$. Similarly, for the second group of light curve parts we measured $\Delta t_{dif,\ median}$ for different bin size values between 3.5 and 4.6 days. We found that $\Delta t_{dif,\ median}$ is minimal for $\Delta t_{bin} = 3.98d$. Finally, for the third group in MCG-6–30–15, $\Delta t_{bin} = 12.8d$ minimizes the time difference between the interpolated data points and observations among values of the bin size from 11 to 15 days. The use of this $\Delta t_{bin}$ resulted in light curves with a duration of $\sim 240d$.

For the most of the parts in the Ark 564 light curve, $\Delta t_{j-i,\ median} \sim 4.3d$. We used all of them as one group and we consider light curve parts with $\Delta t_{j-i,\ median} = 0.14$ as the second group. Similarly with MCG-6–30–15, we determined the bin size which minimizes $\Delta t_{dif,\ median}$. For the Group A, $\Delta t_{dif,\ median}$ is minimal at $\Delta t_{bin} = 4.27d$ and for the second group at $\Delta t_{bin} = 0.131d$. Using those values, we were able to create 21, evenly sampled segments in the first group and 17 segments for the second.

The cadence of observation in Mkn 766 light curve is $\sim 4$–$4.5d$ at almost all times. We used all the available segments to estimate time-lags at a wide frequency range. We have tested different values for the bin size from 4–4.5 days. $\Delta t_{bin} = 4.27d$ minimizes the difference between the observations and the interpolated data points and produces 22 segments with $T_s = 111.02d$.

We calculated the time-lags following the `EP16` method to ensure that they follow a Gaussian distribution with known errors. According to `EP16`, time-lags should be estimated using $n_s \geq 20$ pairs of light curve segments. In our case, the number of segments varies between 15–19 in MCG-6–30–15.

For Ark 564, we ended up with 21 segments in the first group and 17 for the second group. In the case of Mkn 766 we used $n_s = 22$ segments. Using these data, we estimated the time-lags at frequencies from $10^{-8}$ to $10^{-5}$Hz. The high frequency limit is set by the fact that we considered time-lags estimates only at $\nu \leq \nu_{Nyq}/3$, to avoid bias due to aliasing. The low frequency limit is set by the duration of the segments.

For MCG-6–30–15 we ended with 12 reliable time-lag estimates from $4 \times 10^{-8} Hz$ to $10^{-6} Hz$. For Ark 564 and Mkn 766 we were able to measure time-lags at 4 frequencies from $10^{-7} Hz$ to $10^{-5} Hz$ and between 1–4 $\times 10^{-7} Hz$ respectively. To reduce the uncertainty in the time-lags estimates, we binned them together and calculate the average of the time-lags inside each bin. Figs. (3.4), (3.7), and (3.9) present the final time-lag spectra for MCG-6–30–15, Ark 564 and Mkn 766. This is the lowest frequency range at which X-ray time-lags have ever been estimated for these sources. We summarize our main results below.

**1.** All estimated time-lags are consistent with zero within 1–2$\sigma$. In the case of the individual time-lags of MCG-6–30–15, almost all of them are consistent with zero within 1$\sigma$. All the individual time-lags of Ark 564 are also consistent with zero within 1$\sigma$. Regarding the average time-lags, they are also consistent with zero within 1$\sigma$. The only exception is the lowest frequency time-lag in the 2–4 vs 4–7 keV case of MCG-6–30–15, which is consistent with zero at 2$\sigma$.

The agreement with zero could be due to the fact that the intrinsic time-lags are small and time-lags errors are large. The coherence between the 2–4 vs 7–10 keV of MCG-6–30–15 and for all the energy bands we examined in Ark 564 is low. The value of the coherence determines the time-lags error and as a result, the errors are very large and the time-lags estimates are in agreement with zero. Another indication which shows that the intrinsic time-lags could indeed be zero, is the number of positive and negative time-lags. Four out of 12 and 5 out of 12 individual time-lags are positive in the 2–4 vs 4–7 keV and in the 2–4 vs 7–10 keV time-lag spectra of MCG-6–30–15, respectively. If the intrinsic time-lags were equal to zero at low frequencies and their distribution is Gaussian, the probability (determined by the binomial distribution; $p = 0.5$) of measuring 4/12 or 5/12 positive time-lags is 12% and 20% respectively. In the case of Ark 564, half of the individual time lags are positive, which is again consistent with the hypothesis of zero intrinsic time-lags. These results show that the intrinsic time-lags of MCG-6–30–15 and Ark 564 could be equal to zero.

On the other hand, we have evidence that the intrinsic time-lags at low frequencies are small, but indeed, non-zero. EP17 observed a turn-over at the lowest sampled frequencies ($< 10^{-4} Hz$) of MCG-6–30–15, which indicate that the time-lags at frequencies below $\sim 10^{-5} Hz$ could be $\sim$ 100–200s between the same band we have used in this work. Also, McHardy et al. (2007) measured the time-lags of Ark 564 and they observed a flattening in the time-lag spectrum at a value of 1000–1500s at frequencies below $5 \times 10^{-5} Hz$. Even if this is the case, we cannot discriminate between a value of zero or such a small value, given the large errors of the time-lags.

**2.** EP17 measured the time-lag spectra of MCG-6–30–15, Ark 564 and Mkn 766 at high frequencies using XMM-NEWTON data. They found that the X-ray continuum time-lags are well fitted by a power-law model with a slope of $\sim -1$. We examined if the extrapolation of EP17 results is consistent with the time-lag estimates at low frequencies measured by *RXTE*. In the case of MCG-6–30–15 and Ark-564 our time-lag estimates are systematically bellow the extrapolation of EP17 model. Based on simulations performed by EP17, we used eq. (3.19) to calculate the time-lag bias in our estimates. The bias is not significant and our estimates are still below the extrapolation. Nevertheless, the time-lags we measured in MCG-6–30–15 and Ark 564 are still consistent with the extrapolation of EP17 model if we consider the uncertainty of the extrapolation of the high frequency time-lag model to low frequencies. However, our results are consistent with the EP17 results because of the very high uncertainty of the EP17 model extrapolation at low frequencies, so we cannot make any firm statement about the reality of this result.

**3.** Mkn 766 is the only source studied by EP17 whose time-lags do not follow a power law with a slope of $\sim -1$. Instead, the slope is consistent with zero, and the time-lags are between 100–200s in the same energy bands we considered in this work. In our case, the average time-lag of all 4 frequencies is $(-7.5 \pm 3.5) \times 10^4 s$ and $(-7.0 \pm 3.5) \times 10^4 s$ in the 2–4 vs 4–7 keV and 2–4 vs 7–10 keV band time-lags respectively. These results are in agreement with the results of EP17 at higher frequencies within $2\sigma$. Our time-lag estimates confirm the peculiar nature of this source. In fact, our results suggest that at low frequencies the intrinsic time-lags may be zero, or even negative, at low frequencies.

**4.** We found that the coherence between the 2–4 vs 4–7 keV and 2–4 vs 7–10 keV bands is rather flat for MCG-6–30–15. First, the coherence between the 2–4 vs 4–7 keV bands is $> 0.9$ at all frequencies and for all groups. The coherence in this case matches the expected value of the sample coherence when the intrinsic coherence is unity. Regarding the 2–4 vs 7–10 keV case, the coherence is between 0.83–0.90, i.e. lower than the 2–4 vs 4–7 keV case. It is smaller than the expected value, when the intrinsic coherence was unity. This supports the hypothesis that the coherence decreases with increasing energy separation, as it was found by EP17.

The 2–4 vs 7–10 keV coherence is smaller thar the 2–4 vs 4–7 keV band coherence in Ark 564 as well. In addition, the sampled coherence is significantly smaller than the sample coherence in MCG-6–30–15, which indicates the intrinsic coherence is smaller than one in this source. Finally, for Mkn 766 we found that the coherence is the same in the 2–4 vs 4–7 keV and the 2–4 vs 7–10 keV band. The value of the coherence varies between 0.3 to 0.9 and it is smaller than the expected value if the intrinsic coherence was one.

**5.** The presence of a warm absorber may contribute to the time-lags we measured in these objects. Warm absorber is an ionized gas along the line of sight to the central engine in AGN, which absorbs X-ray emission from the AGN. Warm absorbers are detected in about half of the Seyfert galaxies. The gas in warm absorbers is ionized either by collisions or by photoionization from high energy photons emitted by the source.

Silva et al. (2016) used XMM-NEWTON data of NGC 4051 and they found that time-lags measured at longer timescales may carry a time delay associated with the gas response to changes in the ionizing source. As a result, the warm absorber will introduce a time delay in the soft energy band with respect to the variations observed at higher energies. These time delays are opposite to the hard continuum lags which are generated by the X-ray source. Therefore, the measured time-lags will be smaller than the intrinsic time-lags of the X-ray source.

This may be true in the case of MCG-6–30–15, Ark 564 and Mkn 766. If the warm absorber indeed affects the low frequency spectra of these sources, it would explain the fact that our estimates are lower than the extrapolation of EP17 model. In fact, EP17 already detected a low-frequency turn-over at $\nu < 10^{-4} Hz$ in the case of MCG-6–30–15 and they suggest that this could be due to the response of the an ionized absorbing gas to the X-ray variations. However, there is no evidence in the *RXTE* spectra that support the presence of warm absorbers that would affect the energy spectrum in MCG-6–30–15 and Ark 564 above 2keV. Regarding Mkn 766, Rivers et al. (2013) have shown evidence that confirm the presence of a warm absorber in this source, so the peculiar time-lags in this object could be due to the effects of warm absorbers.

**6.** Both the observed X-ray variations and the time-lags in X-ray binaries and AGN can be explained by the "propagating fluctuations" model of Kotov et al. (2001) and Arévalo and Uttley (2006). The model is based on the work of Lyubarskii (1997).

According to the model the X-ray source is plane parallel, and is located above and below the accretion disc. The hot material in the corona is also accreting. The model assumes that mass accretions rate fluctuations in the accreting corona are stirred up at each radius and propagate towards the center. Accordingly, X-ray variations arise over a broad range of time-scales. The longer time-scale fluctuations

are produced far away from the center. If the temperature of the corona increases inwards, then the fluctuations will first appear in the softer band (2–4 keV) and then in the harder band (4–7 and 7–10 keV) as they propagate towards the central BH, producing time-lags. The delay between the variations will depend on the diffusion time scale with which the perturbation is propagated.

NGC 4051 is the only other AGN with time-lags measured at such low frequencies between $10^{-7}Hz$ and $10^{-6}Hz$ (Papadakis et al., 2019). If the low frequency X-ray time-lags in NGC 4051, MCG-6–30–15 and Ark 564 were consistent with the extrapolation of the `EP17` model to low frequencies, then the size of the X-ray corona should be very large. For example, frequencies at $\sim 10^{-7}Hz$ in these AGN correspond to frequencies of $\sim 0.05Hz$ in Cyg X-1 (assuming that the BH mass of these AGN is $\sim 10^5$ times larger than the mass of the BH in BHXBs). Recently, Rapisarda et al. (2017), studied the low frequency time-lags (down to $0.05Hz$) in Cyg X-1, assuming the propagation of the fluctuation model. They showed that, if the model is correct, then the radius of the X-ray corona in Cyg X-1 should be $\sim 2500$ gravitational radii. Assuming that the same model is also correct for AGN, we would expect a similar result for AGN as well. However, results from gravitational microlensing suggest much smaller X-ray corona sizes in AGN (see Chartas et al., 2016). Additionally, a physical heating mechanism would be also required for the creations of this hot flow (with temperatures $\sim 10^8$–$10^9K$) at such large radii. This process remains unknown and it is difficult to be explained with the known heating processes in AGN.

# Bibliography


Akylas, A., & Georgantopoulos, I. (2021). The distribution of the coronal temperature in Seyfert 1 galaxies. *arXiv e-prints*, Article arXiv:2108.11337, arXiv:2108.11337.

Arévalo, P., McHardy, I. M., & Summons, D. P. (2008). X-ray variability of the Seyfert 1 Markarian 335: power spectrum and time lags. *MNRAS*, *388*(1), 211–218. https://doi.org/10.1111/j.1365-2966.2008.13367.x

Arévalo, P., Papadakis, I. E., Uttley, P., McHardy, I. M., & Brinkmann, W. (2006). Spectral-timing evidence for a very high state in the narrow-line Seyfert 1 Ark 564. *MNRAS*, *372*(1), 401–409. https://doi.org/10.1111/j.1365-2966.2006.10871.x

Arévalo, P., & Uttley, P. (2006). Investigating a fluctuating-accretion model for the spectral-timing properties of accreting black hole systems. *MNRAS*, *367*(2), 801–814. https://doi.org/10.1111/j.1365-2966.2006.09989.x

Arnaud, K. A., Branduardi-Raymont, G., Culhane, J. L., Fabian, A. C., Hazard, C., McGlynn, T. A., Shafer, R. A., Tennant, A. F., & Ward, M. J. (1985). EXOSAT observations of a strong soft X-ray excess in MKN 841. *MNRAS*, *217*, 105–113. https://doi.org/10.1093/mnras/217.1.105

Chartas, G., Rhea, C., Kochanek, C., Dai, X., Morgan, C., Blackburne, J., Chen, B., Mosquera, A., & MacLeod, C. (2016). Gravitational lensing size scales for quasars. *Astronomische Nachrichten*, *337*(4-5), 356. https://doi.org/10.1002/asna.201612313

Crummy, J., Fabian, A. C., Gallo, L., & Ross, R. R. (2006). An explanation for the soft X-ray excess in active galactic nuclei. *MNRAS*, *365*(4), 1067–1081. https://doi.org/10.1111/j.1365-2966.2005.09844.x

Done, C., Davis, S. W., Jin, C., Blaes, O., & Ward, M. (2012). Intrinsic disc emission and the soft X-ray excess in active galactic nuclei. *MNRAS*, *420*(3), 1848–1860. https://doi.org/10.1111/j.1365-2966.2011.19779.x

Epitropakis, A., & Papadakis, I. E. (2016). Statistical properties of fourier-based time-lag estimates. *Astronomy & Astrophysics*, *591*, A113. https://doi.org/10.1051/0004-6361/201527665

Epitropakis, A., & Papadakis, I. E. (2017). The X-ray continuum time-lags and intrinsic coherence in AGN. *MNRAS*, *468*(3), 3568–3601. https://doi.org/10.1093/mnras/stx612

Ho, L. C., Filippenko, A. V., & Sargent, W. L. W. (1997). A Search for "Dwarf" Seyfert Nuclei. V. Demographics of Nuclear Activity in Nearby Galaxies. *The Astrophysical Journal*, *487*(2), 568–578. https://doi.org/10.1086/304638

Kotov, O., Churazov, E., & Gilfanov, M. (2001). On the X-ray time-lags in the black hole candidates. *MNRAS*, *327*(3), 799–807. https://doi.org/10.1046/j.1365-8711.2001.04769.x

Lusso, E., Comastri, A., Simmons, B. D., Mignoli, M., Zamorani, G., Vignali, C., Brusa, M., Shankar, F., Lutz, D., Trump, J. R., Maiolino, R., Gilli, R., Bolzonella, M., Puccetti, S., Salvato, M., Impey, C. D., Civano, F., Elvis, M., Mainieri, V., ... Riguccini, L. (2012). Bolometric luminosities and Eddington ratios of X-ray selected active galactic nuclei in the XMM-COSMOS survey. *MNRAS*, *425*(1), 623–640. https://doi.org/10.1111/j.1365-2966.2012.21513.x

Lyubarskii, Y. E. (1997). Flicker noise in accretion discs. *MNRAS*, *292*(3), 679–685. https://doi.org/10.1093/mnras/292.3.679

McHardy, I. M., Arévalo, P., Uttley, P., Papadakis, I. E., Summons, D. P., Brinkmann, W., & Page, M. J. (2007). Discovery of multiple Lorentzian components in the X-ray timing properties of the Narrow Line Seyfert 1 Ark 564. *MNRAS*, *382*(3), 985–994. https://doi.org/10.1111/j.1365-2966.2007.12411.x

McHardy, I. M., Papadakis, I. E., Uttley, P., Page, M. J., & Mason, K. O. (2004). Combined long and short time-scale X-ray variability of NGC 4051 with RXTE and XMM-Newton. *MNRAS*, *348*(3), 783–801. https://doi.org/10.1111/j.1365-2966.2004.07376.x

Miyamoto, S., & Kitamoto, S. (1989). X-ray time variations from Cygnus X-1 and implications for the accretion process. *Nature*, *342*(6251), 773–774. https://doi.org/10.1038/342773a0

Nowak, M. A., & Vaughan, B. A. (1996). Phase lags and coherence of X-ray variability in black hole candidates. *MNRAS*, *280*(1), 227–234. https://doi.org/10.1093/mnras/280.1.227

Nowak, M. A., Vaughan, B. A., Wilms, J., Dove, J. B., & Begelman, M. C. (1999). Rossi X-Ray Timing Explorer Observation of Cygnus X-1. II. Timing Analysis. *The Astrophysical Journal*, *510*(2), 874–891. https://doi.org/10.1086/306610

Papadakis, I. E., & Lawrence, A. (1995). A detailed X-ray variability study of the Seyfert galaxy NGC 4051. *MNRAS*, *272*(1), 161–183. https://doi.org/10.1093/mnras/272.1.161

Papadakis, I. E., Nandra, K., & Kazanas, D. (2001). Frequency-dependent Time Lags in the X-Ray Emission of the Seyfert Galaxy NGC 7469. *The Astrophysical Journal*, *554*(2), L133–L137. https://doi.org/10.1086/321722

Papadakis, I. E., Rigas, A., Markowitz, A., & McHardy, I. M. (2019). The long term X-ray time lags of NGC 4051. *MNRAS*, *485*(1), 1454–1459. https://doi.org/10.1093/mnras/stz489

Petrucci, P. .-O., Paltani, S., Malzac, J., Kaastra, J. S., Cappi, M., Ponti, G., De Marco, B., Kriss, G. A., Steenbrugge, K. C., Bianchi, S., Branduardi-Raymont, G., Mehdipour, M., Costantini, E., Dadina, M., & Lubiński, P. (2013). Multiwavelength campaign on Mrk 509. XII. Broad band spectral analysis. *Astronomy & Astrophysics*, *549*, Article A73, A73. https://doi.org/10.1051/0004-6361/201219956

Pottschmidt, K., Wilms, J., Nowak, M. A., Heindl, W. A., Smith, D. M., & Staubert, R. (2000). Temporal evolution of X-ray lags in Cygnus X-1. *Astronomy & Astrophysics*, *357*, L17–L20.

Rapisarda, S., Ingram, A., & van der Klis, M. (2017). Modelling hard and soft states of Cygnus X-1 with propagating mass accretion rate fluctuations. *MNRAS*, *472*(4), 3821–3832. https://doi.org/10.1093/mnras/stx2110

Rees, M. J. (1984). Black Hole Models for Active Galactic Nuclei. *IN: Annual review of astronomy and astrophysics*, *22*, 471–506. https://doi.org/10.1146/annurev.aa.22.090184.002351

Rivers, E., Markowitz, A., & Rothschild, R. (2013). Full Spectral Survey of Active Galactic Nuclei in the Rossi X-ray Timing Explorer Archive. *The Astrophysical Journal*, *772*(2), Article 114, 114. https://doi.org/10.1088/0004-637X/772/2/114

Silva, C. V., Uttley, P., & Costantini, E. (2016). Timing the warm absorber in NGC 4051. *Astronomy and Astrophysics*, *596*, Article A79, A79. https://doi.org/10.1051/0004-6361/201628555

Sriram, K., Agrawal, V. K., & Raghurama Rao, A. (2009). A truncated accretion disk in the galactic black hole candidate source H1743-322. *Research in Astronomy and Astrophysics*, *9*(8), 901–910. https://doi.org/10.1088/1674-4527/9/8/006

# Appendix A: Equation of a line

The linear equation in the case of 2 variables has the following form:

$$y = ax + b \tag{A.1}$$

Let us consider two sets of point $(y_1, x_1)$ and $(y_2, x_2)$. We need to find the linear equation which passes through the previous points.

We put $(y_1, x_1)$ in eq. (A.1):

$$y_1 = ax_1 + b. \tag{A.2}$$

Similarly for $(y_2, x_2)$:

$$y_2 = ax_2 + b. \tag{A.3}$$

Now, we subtract eq. (A.2) from eq. (A.3):

$$y_2 - y_1 = a(x_2 - x_1) \implies a = \frac{y_2 - y_1}{x_2 - x_1}. \tag{A.4}$$

Then,

$$y = \frac{y_2 - y_1}{x_2 - x_1}x + b \tag{A.5}$$

and for $(y_1, x_1)$,

$$y_1 = \frac{y_2 - y_1}{x_2 - x_1}x_1 + b \tag{A.6}$$

we subtract eq. (A.6) from eq. (A.5):

$$y - y_1 = \frac{y_2 - y_1}{x_2 - x_1}(x - x_1) \tag{A.7}$$

We multiply with the term $(x_2 - x_1)$ to cancel the denominator.

$$(x_2 - x_1)y = y_1(x_2 - x_1) + (y_2 - y_1)(x - x_1) \implies \tag{A.8}$$
$$(x_2 - x_1)y = y_1x_2 - \cancel{y_1x_1} + y_2x - y_2x_1 - y_1x + \cancel{y_1x_1} \implies \tag{A.9}$$
$$(x_2 - x_1)y = (x_2 - x)y_1 + (x - x_1)y_2 \tag{A.10}$$

Finally, dividing by $x_2 - x_2$, we obtain

$$y = \frac{x_2 - x}{x_2 - x_1} y_1 + \frac{x - x_1}{x_2 - x_1} y_2 = \frac{x_2 - x}{x_2 - x_1} y_1 + \frac{x_1 - x}{x_1 - x_2} y_2 \tag{A.11}$$

and the error is given by the following equation.

$$\delta y^2 = \left( \frac{x_2 - x}{x_2 - x_1} \delta y_1 \right)^2 + \left( \frac{x_1 - x}{x_1 - x_2} \delta y_2 \right)^2 \tag{A.12}$$